

## RESEARCH ARTICLE

10.1002/2016JA023167

## Special Section:

Major Results From the MAVEN Mission to Mars

## Key Points:

- SWIA provides direct and proxy measurements of solar wind input to Mars
- The Mars-solar wind interaction varies with solar wind conditions and season
- Mars only perturbs the upstream medium weakly, except during radial IMF

## Correspondence to:

J. S. Halekas,  
jasper-halekas@uiowa.edu

## Citation:

Halekas, J. S., et al. (2016), Structure, dynamics, and seasonal variability of the Mars-solar wind interaction: MAVEN Solar Wind Ion Analyzer in-flight performance and science results, *J. Geophys. Res. Space Physics*, 121, doi:10.1002/2016JA023167.

Received 14 JUL 2016

Accepted 31 AUG 2016

Accepted article online 3 SEP 2016

## Structure, dynamics, and seasonal variability of the Mars-solar wind interaction: MAVEN Solar Wind Ion Analyzer in-flight performance and science results

J. S. Halekas<sup>1</sup>, S. Ruhunusiri<sup>1</sup>, Y. Harada<sup>2</sup>, G. Collinson<sup>3</sup>, D. L. Mitchell<sup>2</sup>, C. Mazelle<sup>4</sup>, J. P. McFadden<sup>2</sup>, J. E. P. Connerney<sup>3</sup>, J. R. Espley<sup>3</sup>, F. Eparvier<sup>5</sup>, J. G. Luhmann<sup>2</sup>, and B. M. Jakosky<sup>5</sup>

<sup>1</sup>Department of Physics and Astronomy, University of Iowa, Iowa City, Iowa, USA, <sup>2</sup>Space Sciences Laboratory, University of California, Berkeley, California, USA, <sup>3</sup>NASA Goddard Space Flight Center, Greenbelt, Maryland, USA, <sup>4</sup>L'Institut de Recherche en Astrophysique et Planétologie, Toulouse, France, <sup>5</sup>Laboratory for Atmospheric and Space Physics, University of Colorado Boulder, Boulder, Colorado, USA

**Abstract** We report on the in-flight performance of the Solar Wind Ion Analyzer (SWIA) and observations of the Mars-solar wind interaction made during the Mars Atmosphere and Volatile Evolution (MAVEN) prime mission and a portion of its extended mission, covering 0.85 Martian years. We describe the data products returned by SWIA and discuss the proper handling of measurements made with different mechanical attenuator states and telemetry modes, and the effects of penetrating and scattered backgrounds, limited phase space coverage, and multi-ion populations on SWIA observations. SWIA directly measures solar wind protons and alpha particles upstream from Mars. SWIA also provides proxy measurements of solar wind and neutral densities based on products of charge exchange between the solar wind and the hydrogen corona. Together, upstream and proxy observations provide a complete record of the solar wind experienced by Mars, enabling organization of the structure, dynamics, and ion escape from the magnetosphere. We observe an interaction that varies with season and solar wind conditions. Solar wind dynamic pressure, Mach number, and extreme ultraviolet flux all affect the bow shock location. We confirm the occurrence of order-of-magnitude seasonal variations of the hydrogen corona. We find that solar wind Alfvén waves, which provide an additional energy input to Mars, vary over the mission. At most times, only weak mass loading occurs upstream from the bow shock. However, during periods with near-radial interplanetary magnetic fields, structures consistent with Short Large Amplitude Magnetic Structures and their wakes form upstream, dramatically reconfiguring the Martian bow shock and magnetosphere.

## 1. Introduction

The goals of the Mars Atmosphere and Volatile Evolution (MAVEN) mission [Jakosky et al., 2015a] are to characterize the present-day structure and dynamics of the Martian atmosphere, ionosphere, and magnetosphere and to measure the loss rate of atmospheric gases from this coupled system, enabling an extrapolation over time to determine the integrated loss of atmosphere from Mars over solar system history. To achieve these goals, we must understand not only the current Martian system but also the physics of the processes therein and how those processes depend on season, local time, geographic location, external drivers, etc. Without a full understanding of how the Martian system depends on solar drivers, we have little hope of performing a robust extrapolation back in time. Underscoring the importance of this goal, five of the nine sensors on the MAVEN spacecraft measure portions of the energy input from the Sun, including extreme ultraviolet (EUV) photons, thermal ions and electrons, suprathermal ions and electrons, solar energetic particles, and the interplanetary magnetic field (IMF). The Solar Wind Ion Analyzer (SWIA) [Halekas et al., 2015a], designed to measure the 3-D velocity distribution of solar wind ions both upstream and downstream from the Martian bow shock, falls into this category.

The solar wind provides a highly variable source of energy to the Martian system. Under nominal conditions, the solar wind flow speed can vary by a factor of 2, and the density can vary over an order of magnitude. Stream interactions such as corotating interaction regions (CIRs) and space weather events such as coronal mass ejections (CMEs) can introduce even larger perturbations. While the properties of the solar wind do not differ dramatically between 1 AU and Mars, only when Mars and the point of solar wind observation lie within  $\sim 65^\circ$  in heliocentric longitude can one propagate measurements to Mars with any degree of reliability

[Opitz *et al.*, 2010]. Even during times with such fortuitous alignment, stream interaction regions can merge and/or steepen dramatically between 1 and 1.5 AU [Burlaga *et al.*, 1985; Gosling and Pizzo, 1999]. To fully understand the response of Mars to the solar wind during the MAVEN mission, we therefore require a dedicated solar wind monitor.

A number of previous investigations have suggested that the solar wind in part controls the loss of ions from the atmosphere of Mars. Studies utilizing data from different times in the solar cycle imply different ion escape rates. Phobos-2 measurements during an intense solar maximum [Lundin *et al.*, 1990; Ramstad *et al.*, 2013] indicate higher escape fluxes than more recent measurements from Mars Express (MEX) [Barabash *et al.*, 2007] and MAVEN [Brain *et al.*, 2015] for similar ion energy ranges during more moderate solar wind conditions. However, the exact nature of the dependence of ion loss rate on solar wind parameters remains unclear. Event studies suggest that CMEs and CIRs can both lead to enhanced ion escape [Dubinin *et al.*, 2009; Edberg *et al.*, 2010b; Futaana *et al.*, 2008; Jakosky *et al.*, 2015b], implying that increased solar wind flux drives enhanced ion loss. However, statistical studies do not all support this conclusion, with some finding increased ion escape during high solar wind flux periods [Nilsson *et al.*, 2011] but others finding a non-monotonic dependence of escape rates on solar wind density [Ramstad *et al.*, 2015].

Given the number of possible pathways for ion escape from Mars [see, e.g., Dubinin *et al.*, 2011], some nonlinearity in the dependence of total ion loss rates with solar wind parameters should naturally result. Each individual escape process will, in general, scale in a different way, and therefore, under different solar wind conditions the dominant loss process could change. The solar wind can transfer momentum to the planetary ions to give them escape velocity in many different ways, including but not limited to direct acceleration by the motional electric field (“pickup”) [Dubinin *et al.*, 2006b; Dong *et al.*, 2015], which transitions to “heavy mass-loading” or “mass-loaded pickup” in regions of higher planetary ion density [Lundin *et al.*, 1991],  $\mathbf{J} \times \mathbf{B}$  acceleration in the tail [Dubinin *et al.*, 1993a], cold plasma outflow [Lundin *et al.*, 2008; Fraenz *et al.*, 2015], shear-driven boundary layer instabilities [Penz *et al.*, 2004; Gunell *et al.*, 2008; Winningham *et al.*, 2006], wave-driven acceleration [Ergun *et al.*, 2006], and bulk escape of “plasma clouds” [Halekas *et al.*, 2016]. Plasma energization can also couple back into heating of the neutral atmosphere, leading to secondary loss terms [Luhmann and Kozyra, 1991; Leblanc and Johnson, 2001]. Work remains to determine how ions escape from Mars by this diverse array of loss processes, how the total ion loss depends on the driving solar wind input to the system, and how that dependence varies with other factors such as season, geographic location, and local time.

To reach closure on the scientific goals of the MAVEN mission, we therefore must comprehensively measure the properties of the incoming solar wind at Mars. SWIA fulfills this role, providing high-fidelity measurements of the solar wind input to the Martian system. In this paper, we describe the in-flight performance of the as-flown SWIA instrument in the near-Mars environment and discuss some new insights obtained from SWIA measurements of the properties of the solar wind at Mars and the Mars-solar wind interaction.

## 2. MAVEN Solar Wind Ion Analyzer (SWIA) Measurements and In-Flight Performance

### 2.1. Instrument Characteristics

The MAVEN/SWIA instrument [Halekas *et al.*, 2015a], based on the classic Carlson *et al.* [1983] top-hat design, consists of a toroidal electrostatic analyzer with electrostatic deflectors that measures ions over an energy range of  $\sim 5$ –25,000 eV, over a maximum angular range of  $360^\circ \times 90^\circ$  (smaller at energies above 4.5 keV). SWIA does not discriminate between ion species but does provide intrinsic energy resolution of 15%  $\Delta E/E$ , angular resolution of  $22.5^\circ \times 22.5^\circ$  over the full  $360^\circ \times 90^\circ$  field of view (FOV), with  $4.5^\circ \times 3.75^\circ$  over a  $45^\circ \times 45^\circ$  portion of the FOV nominally covering the solar wind, and 4 s intrinsic time resolution. SWIA is mounted on a corner of the main spacecraft deck, providing a largely open field of view and aligning its fine resolution elements toward the Sun whenever the spacecraft  $Z$  axis points toward the Sun (true for the majority of observational modes). Early in the MAVEN mission (November 2014), issues with spacecraft charging at periaresis forced a change in the SWIA energy coverage to 25–25,000 eV, to protect the detectors from intense low-energy ram fluxes postaccelerated by the negative spacecraft potential. This issue notwithstanding, SWIA has operated nominally throughout the MAVEN mission to date, as well as for 4 months during cruise to Mars (March–July 2014), providing a comprehensive data set of the solar wind beyond 1 AU and its interaction with Mars.

## 2.2. Data Products, Modes, and Operations

The SWIA sensor operates continuously in a single mode, accumulating counts over 96 energy steps (“E”) covering the full energy range and 24 deflection steps (“D”) covering instrument theta angles of  $\pm 45^\circ$ , for each of 24 anodes (“A”) that together cover instrument phi angles of  $0\text{--}360^\circ$  (14 large anodes with  $22.5^\circ$  angular extent and 10 small anodes with  $4.5^\circ$  angular extent covering a portion of the FOV centered around the spacecraft Z axis, nominally oriented toward the Sun). The resulting product (P0) is too big to send routinely, so the SWIA firmware processes this basic array into two more compact forms, as described in *Halekas et al.* [2015a]. The “Coarse 3-D” (P1) product sums pairs of adjacent energy steps, sums groups of six deflector steps, and sums over two groups of five small anodes, to produce a  $48\text{E} \times 16\text{A} \times 4\text{D}$  distribution covering the full energy and angular range with a uniform 15% energy resolution and  $22.5^\circ \times 22.5^\circ$  angular resolution. The “Fine 3-D” (P2) product selects the deflector steps and energy steps around the peak in the distribution for the 10 small anodes to produce a  $48\text{E} \times 10\text{A} \times 12\text{D}$  distribution covering a limited portion of phase space with 7.5% energy resolution (oversampled compared to the intrinsic resolution) and  $4.5^\circ \times 3.75^\circ$  angular resolution. The flight software (FSW) in the data processing unit then transfers these products directly to the spacecraft as “Survey” data and/or to the “Archive” flash memory for later selection and transmission or further bins or subselects to produce smaller products before transferring them to one of these two destinations. The FSW also sums over all angles to collapse the Coarse 3-D product to an “Onboard” 1-D energy spectrum, computes the moments ( $n$  = density,  $\mathbf{v}$  = vector velocity,  $\mathbf{p}$  = pressure tensor,  $\mathbf{Q}$  = vector heat flux) of the distribution, and controls a mechanical attenuator based on peak count rate. Though the instrument operates in a single mode, FSW utilizes the ratio of counts contained in the Coarse and Fine distributions (a measure of narrowness of the distribution) to determine a telemetry mode (“Sheath” or “Solar Wind”). This mode bit also determines whether the FSW utilizes Coarse or Fine distributions to compute moments. The resulting combination of data products provides a powerful data set for studying the Mars-solar wind interaction, but care is required to appropriately utilize all the data products and correctly interpret data taken with different telemetry modes and attenuator states.

## 2.3. Interpreting SWIA Measurements

Figure 1 shows a representative example of SWIA measurements from a single MAVEN orbit in February 2015. During this orbit, outside of the bow shock (before  $\sim 18:20$  and after  $\sim 20:50$ ), SWIA measured the nearly pristine solar wind proton ( $\text{H}^+$ ) and alpha particle ( $\text{He}^{++}$ ) populations. These two populations appear as clearly distinct peaks in the Fine energy spectra of Figure 1e (also visible at lower energy resolution in the Onboard and Coarse energy spectra of Figures 1a and 1b), separated by a factor of roughly 2 in energy per charge due to their nearly equal flow speeds but different mass to charge ratios (1:1 for protons as compared to 4:2 for alphas).

In addition to the incoming solar wind, MAVEN encountered a number of other ion populations labeled in Figure 1a, including (1)  $\text{H}^+$  pickup ions produced from the exosphere (see Figure 1e for clearest view) [Dubinin et al., 2006b], (2) penetrating hydrogen near periapsis [Kallio and Barabash, 2001; Halekas et al., 2015c; Bougher et al., 2015], (3) accelerated heavy ions near the magnetotail current sheet [Dubinin et al., 1993a; DiBraccio et al., 2015], (4) energetic  $\text{O}^+$  pickup ions produced from the distant corona [Rahmati et al., 2015], and (5) reflected protons from the bow shock [Dubinin et al., 2006b]. To identify these populations, we utilized contextual information from Suprathermal and Thermal Ion Composition (STATIC) and Magnetometer (MAG) (not shown).

To understand the details of the SWIA measurements in Figure 1, we need to take into account a number of factors. First, we consider the telemetry mode and the mechanical attenuator status, both autonomously set on board by the FSW. The telemetry mode determines the mix of data products, with Fine distributions only returned in the Survey stream in Solar Wind mode (later in the mission, the Archive data stream included some Fine distributions even in Sheath mode). During the orbit shown in Figure 1, the automatic mode selection worked mostly as intended, with the telemetry mode set to Solar Wind for time periods outside the bow shock, ensuring the return of more Fine distributions appropriate for resolving narrow solar wind proton and alpha particle distributions, while inside the bow shock the Sheath telemetry mode ensured the return of more Coarse distributions appropriate for characterizing the heated distributions in the sheath. However, from 20:04 to 20:22, the telemetry mode also briefly switched to Solar Wind, despite the spacecraft location in the sheath. Since changes in the telemetry mode also change

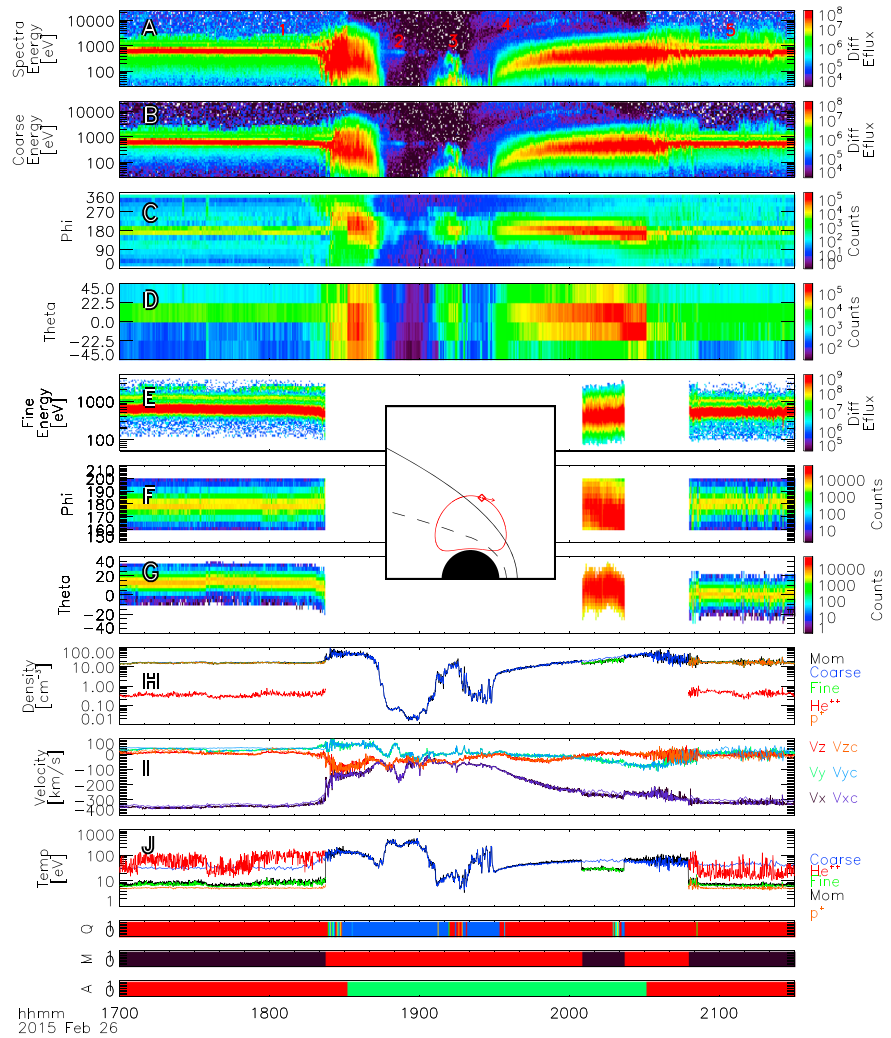


**Figure 1.** Solar Wind Ion Analyzer (SWIA) observations from a representative MAVEN orbit. (a) The onboard-computed energy spectra. (b–d) The spectra show energy per charge, instrument phi angle, and instrument theta angle projections, computed on the ground from the Coarse 3-D data product. (e–g) The spectra show energy per charge, phi, and theta projections computed from the Fine 3-D data product. For both products, we display energy spectra in units of differential energy flux [eV/(eV cm<sup>2</sup> s sr)], while phi and theta spectra show raw counts. (h–j) Comparisons of onboard moments (“Mom”) to ground moments computed from the Coarse and Fine distributions, as well as the results of a two-component analysis that determines separate moments for protons (“p<sup>+</sup>”) and alpha particles (“He<sup>++</sup>”). The velocity comparison shows [V<sub>x</sub>, V<sub>y</sub>, V<sub>z</sub>] from onboard moments and [V<sub>x<sub>c</sub></sub>, V<sub>y<sub>c</sub></sub>, V<sub>z<sub>c</sub></sub>] computed from Coarse distributions. All vector quantities utilize Mars Solar Orbital (MSO) coordinates [Vignes *et al.*, 2000]. The three color panels at the bottom of the plot show the quality flag for the onboard moments (red = best, blue = worst), the telemetry mode (black = solar wind, red = sheath), and the mechanical attenuator state (green = open, red = closed). The inset shows the cylindrical projection of the spacecraft position for this orbit in MSO coordinates, with the start point and spacecraft velocity direction shown by the diamond and arrow. The solid and dashed black curves on the inset show the nominal bow shock and magnetic pileup boundary location from Trotignon *et al.* [2006]. The numbers 1–5 in Figure 1a indicate ion populations of interest described in the text.

the source of the onboard moment computation, we must take some care in interpreting the onboard moments near mode switches, since they can introduce nonphysical discontinuities. Generally, mode switches only have minor effects on density and velocity moments (Figures 1h and 1i), but the temperature moment (Figure 1j) shows much more significant effects, since the resolution of the measurement significantly limits the temperature computation, particularly for a narrow distribution like the solar wind. Resolving the off-axis velocity components of a narrow distribution such as the solar wind also requires the use of moments computed in Solar Wind mode.

The mechanical attenuator state also affects the data. When engaged, the attenuator reduces the sensitivity over the sunward facing portion of the FOV, with a maximum attenuation factor of 15 for an instrument phi range of  $\pm 45^\circ$  from the spacecraft Z axis, and incrementally reduced attenuation at greater angles [see Halekas *et al.*, 2015a]. When looking at Coarse data in units of counts (e.g., Figures 1c and 1d), this attenuation applied to an ion distribution that decreases with phi angle from the antisunward direction produces a characteristic “W” shape in the sunward portion of the phi angle count spectrum. Generally, this has few adverse effects, since the FSW accounts for this change in sensitivity when computing onboard moments, and publicly available ground analysis software accounts for this sensitivity change when computing any quantities from the 3-D distributions in physical units (e.g., Figures 1a, 1b, and 1e). Therefore, the attenuator actuation typically does not create any noticeable discontinuities in the data. However, the variable sensitivity can complicate the interpretation of narrow features that lie in regions of phase space with a nonconstant attenuation factor (i.e., near the edges of the attenuated phi angle range). In addition, the attenuator can have visible effects on the onboard energy spectra (Figure 1a), since these sum counts over all angles, thereby combining measurements made with different sensitivities for times with the attenuator engaged. The ground software by default assumes that all counts in the spectra from times with the attenuator engaged lie in the fully attenuated portion of the FOV (a reasonable assumption since the attenuator usually only engages in the solar wind). This assumption works well but has the effect of artificially increasing the weight of any background counts or counts that lie outside of the attenuated portion of the FOV. Thus, we often find an artificial step in the apparent background in the energy spectra at the attenuator transition.

#### 2.4. Sources of Error and Uncertainty in SWIA Measurements

While the factors discussed above affect the interpretation of the SWIA data, they do not necessarily lead to errors (though they can in some cases). However, we must now discuss several additional effects that do, in general, lead to measurement errors. First, several nonphysical sources of counts exist. Energetic cosmic rays (or solar energetic particles) can penetrate the instrument housing and stimulate the detectors, creating a uniform background present over all accumulation intervals (not varying with energy or deflection step). Except during major energetic particle events, these penetrating particles produce spurious counts with a rate of only a few hertz over the entire sensor. For nominal solar wind and sheath conditions this background proves completely negligible, but in regions of the magnetosphere with few ions present in the SWIA energy range (e.g., near time “2” in Figure 1), this background can affect moment calculations. The uniform background artificially reduces the magnitude of the velocity moment while increasing the density and the temperature moments.

A second background source results from scattering of solar wind ions from the spacecraft bus and instrument surfaces. For typical solar wind energies,  $< \sim 1\%$  of the incident ions scatter in charged form from a typical surface, so we can often neglect this background. However, the intense fluxes of the solar wind create a measurable scattered background for energies at and below the solar wind energy, as seen in Figures 1a–1d. The angular distribution of this background indicates that it comes from the instrument internal and external surfaces (with a large contribution at  $180^\circ$  instrument phi angle resulting from scattering from a portion of the aperture blocked by instrument harnessing and the harness cover) and from the spacecraft bus (the FOV near  $90^\circ$  instrument phi angle contains the largest contribution from the spacecraft). This scattered population only slightly affects computed moments for the solar wind but can complicate the investigation of minority ion populations (such as pickup ions) when they have energies below that of the solar wind. The orbit shown in Figure 1, with a very high solar wind density, demonstrates a “worst-case” scattered ion population.

Another form of error arises from incomplete coverage of phase space. Though SWIA has very broad FOV and energy coverage, in its current operational mode it does not measure energies below 25 eV, and it has two “blind spots” at high instrument theta angles that together cover  $\sim 30\%$  of the sky (more at high energies). Given the nominal sunward alignment of the instrument, SWIA rarely misses any of the primary solar wind population (only during communications orbits and only then for very unfavorable Sun–Earth angles). However, in the sheath and magnetosphere, SWIA can and does miss portions of the distribution. In fact, in the ionosphere, most of the ion density lies out of the SWIA energy range, and researchers should instead use STATIC data to investigate the bulk distribution. While one cannot determine a priori what lies

in the portion of phase space not covered, we can utilize computed moments to estimate whether the component that we do observe mainly lies in the measured portion. By comparing the portion of phase space within one thermal width of the location of peak flux to the measured portion of phase space, we construct a quality flag that indicates when the onboard moments cover the distribution adequately. This quality flag, shown at the bottom of Figure 1, provides a first-order measure of when one can likely trust the onboard moment computation.

However, the quality flag does not (and cannot) account for another major source of error in SWIA measurements—namely, the presence of more than one ion species. SWIA measures flux, which remains valid regardless of ion mass. However, any derived quantities (i.e., moments) require an assumption as to the ion mass. In the case of the onboard-computed and most ground-computed moments, the calculations assume that all ions are protons. This provides a good approximation in the solar wind and magnetosheath, which typically consist of >90% protons. However, in the magnetosphere, this provides a very poor approximation to reality. Given heavy ions of mass  $M$  (typically  $\sim 16$ – $32$  in the magnetosphere), moment computations that assume protons will overestimate velocity moments by a factor of  $\sqrt{M}$ , underestimate density moments by a factor of  $\sqrt{M}$ , and overestimate temperature moments by a factor of  $M$ .

In the solar wind, though the trace presence of alpha particles barely affects the density and velocity moments, they do artificially increase the temperature moment (by a factor of  $\sim 2$  in  $T_x$ ), due to their higher energy per charge. Therefore, one should never use SWIA onboard-computed solar wind temperature moments for quantitative purposes. Instead, one should utilize the publicly available ground software to compute separate proton and alpha particle moments. This software, which utilizes the Fine 3-D distributions, bisects the measured distribution at the minimum in count rate between the proton and alpha peaks and computes separate moments for the two portions of the distribution (assuming that the two peaks consist of protons and alphas). As shown in Figures 1h–1j, this provides much better resolution of the proton temperature, as well as separate characterization of the alpha particle population. The computation assumes the presence of only two particle populations, so when other populations (e.g., the  $H^+$  pickup ions at time 1 in Figure 1) also contribute, even this method can result in errors. Furthermore, for very cold solar wind ion distributions, even a two-moment analysis returns artificially large temperature estimates, because the finite energy-angle resolution of the instrument becomes important.

Despite the potential interpretational issues and measurement errors described above (many of which apply to all solar wind instruments), SWIA returns excellent measurements of the solar wind and its interaction with the Martian system, provided that one utilizes each data product only where appropriate.

### 2.5. SWIA Measurements in Context

Several experiments have previously measured solar wind ion fluxes at Mars, notably including the Ion and Electron Spectrometer (HARP) [Szucs *et al.*, 1990], Proton and Alpha Particle Spectrometer (TAUS) [Rosenbauer *et al.*, 1989], and Analyzer of Space Plasmas and Energetic Atoms (ASPERA) [Lundin *et al.*, 1989] instruments on Phobos-2 and the MEX ASPERA-3 experiment [Barabash *et al.*, 2006]. Of these, the TAUS instrument came closest to the dedicated solar wind sensor that SWIA represents, with the others more focused on measurements of heavy ions in the Martian magnetosphere. These experiments provide important context for the MAVEN measurements.

On MAVEN, a number of other instruments provide complementary measurements to those from SWIA. The Suprathermal and Thermal Ion Composition (STATIC) sensor [McFadden *et al.*, 2015], designed to measure heavy ions in the magnetosphere, covers energies below 25 eV (in addition to the SWIA energy range) and provides mass composition information at all energies. STATIC makes high-quality measurements in the magnetosphere, but it can saturate in the intense solar wind, and the articulated payload platform on which it resides does not typically place it in an optimal orientation for measuring the solar wind, so SWIA measurements play a unique and important role in MAVEN science. At times when both STATIC and SWIA make good measurements (primarily in the magnetosheath), the two independently calibrated sensors agree very well. Also on MAVEN, the Extreme Ultraviolet Monitor (EUVM) [Eparvier *et al.*, 2015], the Solar Wind Electron Analyzer (SWEA) [Mitchell *et al.*, 2016], the solar energetic particle (SEP) investigation [Larson *et al.*, 2015], and the Magnetometer (MAG) [Connerney *et al.*, 2015a, 2015b] provide EUV photon fluxes, solar wind electron fluxes, energetic particle fluxes, and magnetic field values.

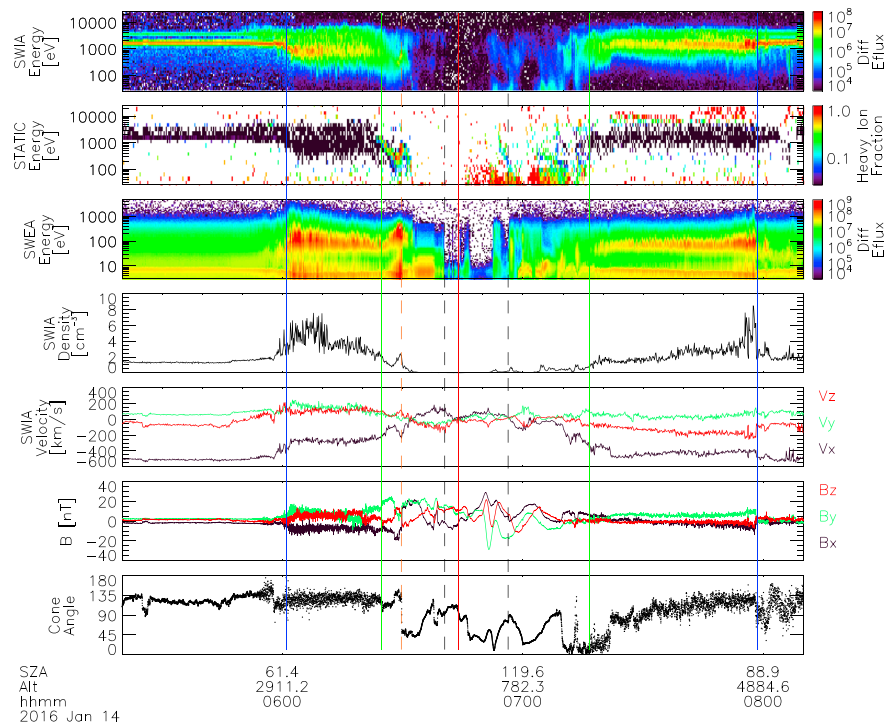


**Figure 2.** MAVEN measurements from a passage through Mars' magnetosphere, showing SWIA Coarse ion energy spectra in  $\text{eV}/(\text{eV cm}^2 \text{ s sr})$ , heavy ion fraction (1 = 100%) from STATIC, SWEA electron energy spectra in  $\text{eV}/(\text{eV cm}^2 \text{ s sr})$ , density and velocity moments computed from SWIA Coarse 3-D distributions, and the magnetic field vector components and the cone angle  $\cos^{-1}(B_x/|B|)$  from MAG. All vector quantities utilize MSO coordinates. Blue lines show the approximate bow shock position, green lines show the approximate induced magnetosphere boundary (IMB) position, the dashed orange line shows the current sheet, the red line marks periapsis, and the dashed black lines show the shadow boundary at spacecraft altitude. Text labels indicate solar zenith angle ("SZA") and altitude ("Alt") in km.

Figures 2 and 3 show a selection of SWIA observations and complementary measurements from STATIC, SWEA, and MAG from corresponding portions of two consecutive orbits on 14 January 2016 that demonstrate the overall structure and variability of the Mars-solar wind interaction as seen by MAVEN. The Martian system [Nagy et al., 2004; Dubinin et al., 2008; Mazelle et al., 2004] consists of an upstream region (including the fore-shock), a bow shock, a magnetosheath region filled with shocked and heated plasma and draped magnetic fields primarily of solar wind origin, and an inner magnetosphere and ionosphere dominated by planetary ions and a mix of induced and crustal magnetic fields [Acuña et al., 1999]. The boundary (or boundaries) between the sheath and the magnetosphere separate a region of turbulent magnetic fields from a region with typically stronger and more steady fields (the "magnetic pileup boundary" (MPB)) and also separate plasma of solar wind origin from plasma of planetary origin (the "ion composition boundary" or ICB, also known as the "induced magnetospheric boundary" (IMB) or even just the "magnetospheric boundary" (MB)) [Bertucci et al., 2005; Brain et al., 2005; Nagy et al., 2004; Dubinin et al., 2006a; Trotignon et al., 2006; Verigin et al., 1993, 1999; Vignes et al., 2000].

The orbit shown in Figure 2 took place during relatively steady IMF conditions, with a nominal  $+B_y/-B_x$  Parker spiral geometry. However, the interaction still displays complex structure. Outside of the bow shock, large-amplitude Alfvén waves exist, as apparent from correlated velocity and magnetic field fluctuations. We will discuss these structures further in section 5. Near but still upstream of the bow shock, the level of fluctuations increases and they become compressional, commensurate with the appearance of additional ion populations formed by reflected protons (above the solar wind energy on the inbound segment outside the bow shock, below on the outbound segment, and right at the bow shock on the inbound segment). On the inbound segment, these reflected protons correlate with an extended "foot" region. We also find a clear "overshoot," most apparent on the outbound segment, with large-amplitude oscillations in density near the shock. Given the observed IMF ( $+B_y/-B_x$ ) and the apoapsis on the  $+Y$  side of Mars, one would expect a

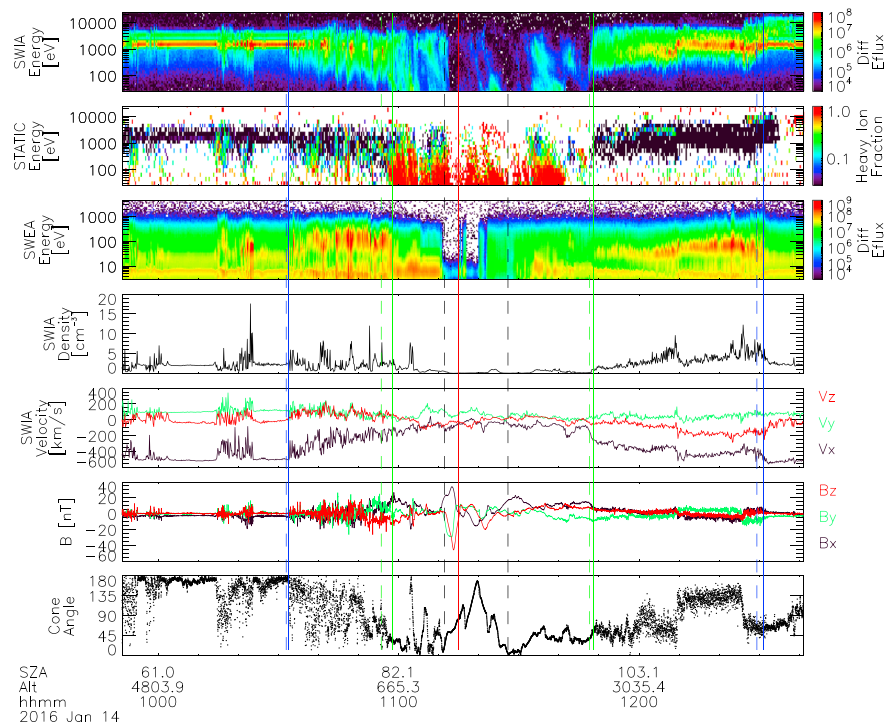


**Figure 3.** MAVEN measurements from a passage through the Martian magnetosphere, in the same format as Figure 2, for the succeeding orbit. Dashed lines show the boundary positions from the preceding orbit (same time from periapsis), and solid lines show the approximate boundary positions for this orbit.

quasi-perpendicular geometry for both inbound and outbound bow shock crossings, and MAVEN observations appear consistent with this expectation.

Inside the bow shock, the sheath contains heated protons and electrons primarily of solar wind origin, with significant compressive (the magnitude of  $B$  and  $n$  change) turbulent fluctuations apparent in the density, velocity, and field components. The electrons appear well thermalized, but the protons retain some multi-component structure even at the inner edge of the sheath, consistent with previous observations indicating incomplete thermalization [Dubinin *et al.*, 1993b]. In the sheath protons dominate the composition, but STATIC also measures trace populations of heavy ions, primarily at energies above the main sheath population, indicative of accelerated pickup ions. Low count rates at the solar wind energy represent straggling from internally scattered protons in the STATIC instrument. Very low count rates of low-energy heavy ions in the solar wind and sheath most likely represent sputtered material from the spacecraft, given the energy distribution very different from that expected from atmospheric/exospheric ions.

At the inner boundary of the sheath the density, velocity, and magnetic field fluctuations all diminish, and the majority ion composition transitions from protons to heavy ions. Inside this boundary, one should not utilize the SWIA moments for quantitative purposes. In locations in sunlight, this compositional change correlates with a shift in observed electron distributions toward an ionospheric spectrum. In shadow suprathermal electrons disappear almost entirely in some locations (“electron voids” or “suprathermal electron depletions”), while other regions have a more sheath-like spectrum (“flux spikes”), reflecting the effects of the complex magnetic topology around crustal magnetic field sources [Brain *et al.*, 2007; Steckiewicz *et al.*, 2015]. Ion fluxes appeared lower, but not entirely absent, in void regions.

On the inbound segment MAVEN crossed the induced current sheet, a region surrounded by heated electrons and accelerated planetary ions. On the outbound segment, farther downstream along the flank, the transition from magnetosphere to sheath proves much less distinct, with intermixed solar wind and planetary ions, and highly accelerated heavy ion populations, a few with apparent energy-time dispersion that may result from nonlocal acceleration of heavy ions [Halekas *et al.*, 2015b]. These accelerated ions appear in

regions with a wide range of suprathermal electron fluxes, suggesting that they cross magnetic field lines, as expected given their large gyroradii.

Figure 3 shows a corresponding portion of the succeeding orbit, 4 h and 31 min after the time segment shown in Figure 2. In the intervening time, the IMF changed from a Parker spiral orientation to a radial configuration dominated by  $B_x$ , indicating that the inbound shock crossing should have a quasi-parallel geometry. This rotation in the IMF has a dramatic change in both the upstream region and the magnetosphere, similar to the effects seen at Venus for radial IMF [Zhang *et al.*, 2009]. Upstream of the bow shock, sporadic large amplitude fluctuations in the density, velocity, and magnetic field appear. These compressive features, some interspersed with heated but more tenuous ion and electron populations, have amplitudes comparable to the bow shock but lie well outside of the nominal bow shock location. Some of the heated plasma contains small admixtures of heavy ions, suggesting at least sporadic access to the Martian magnetosphere. Even taking into account the heavy ion content, these regions have lower charge and mass density than the surrounding solar wind, as well as lower magnetic field, suggesting that thermal pressure must make up the difference. We will discuss some possibilities for their origin in section 5.

Inside the bow shock, the sheath also contains higher amplitude fluctuations than on the previous orbit, as well as interspersed heated but more tenuous populations containing an appreciable fraction of heavy ions, much like those seen outside the bow shock, but with higher heavy ion content. These regions have total mass density comparable to or less than the solar wind, total charge density less than the solar wind, and lower values of both charge and mass density than the surrounding sheath regions. The heavy ion content of these structures indicates that they cannot simply represent structures convected from upstream through the sheath. Instead, the interspersed populations with solar wind and magnetospheric origins must indicate either complex spatial structure or large amplitude fluctuations in the position of the boundary. These could represent shear-driven instabilities such as Kelvin-Helmholtz [Penz *et al.*, 2004] and/or bulk loss of clouds of magnetosphere plasma [Halekas *et al.*, 2016]. Inside the magnetosphere, energy-time dispersed ions [Halekas *et al.*, 2015b] appear throughout the magnetosphere, suggesting acceleration by significant electric fields, possibly associated with the upstream and/or sheath dynamics. On the outbound segment, the IMF rotates away from a radial configuration, and the sheath and upstream region return to a more typical configuration.

Despite the complex structure and dynamics revealed during these two orbits, including large amplitude fluctuations in the upstream region, sheath, and magnetosphere, the main boundaries of the magnetosphere appear relatively constant in location. Therefore, though locally huge perturbations may occur, we can still usefully consider the basic structure of the magnetosphere in a single framework, at least in an average sense. In the next two sections, we will discuss SWIA measurements of the solar wind input to the system, the structure of the magnetosphere, and its variability with solar wind conditions.

### 3. Solar Energy Inputs to the Martian System

#### 3.1. Upstream Measurements of the Solar Wind

To characterize the upstream solar wind that in part drives the Martian system, we utilize SWIA onboard moments and MAG measurements. In order to avoid contamination from measurements taken inside the bow shock, one could in principle utilize at least two different approaches. One could determine a maximum bow shock size and then utilize only data points from outside of that surface. However, we found this approach undesirable, since the MAVEN orbit often does not extend far beyond the bow shock (sometimes, not at all), and a conservative maximum bow shock surface would eliminate a large fraction of the available upstream observations. Furthermore, even defining points safely outside the bow shock does not necessarily remove contamination from the foreshock, which can greatly perturb the upstream flow, particularly during periods with radial IMF (see, e.g., Figure 3).

Therefore, we instead chose to utilize an algorithm based on the measured bulk flow speed  $|\mathbf{v}|$ , proton scalar temperature  $T$ , altitude  $R$ , and normalized magnetic field fluctuation levels  $\sigma_B/|\mathbf{B}|$  (here  $\sigma_B$  represents a root-sum-squared value of the 32 Hz fluctuation levels in all three components over a 4 s interval) to select undisturbed solar wind intervals. We tuned this algorithm based on observations and determined that points with  $|\mathbf{v}| > 200$  km/s,  $\sigma_B/|\mathbf{B}| < 0.15$ ,  $R > 500$  km, and  $\sqrt{T}/|\mathbf{v}| < 0.012$  reliably lie in the pristine solar wind. The last

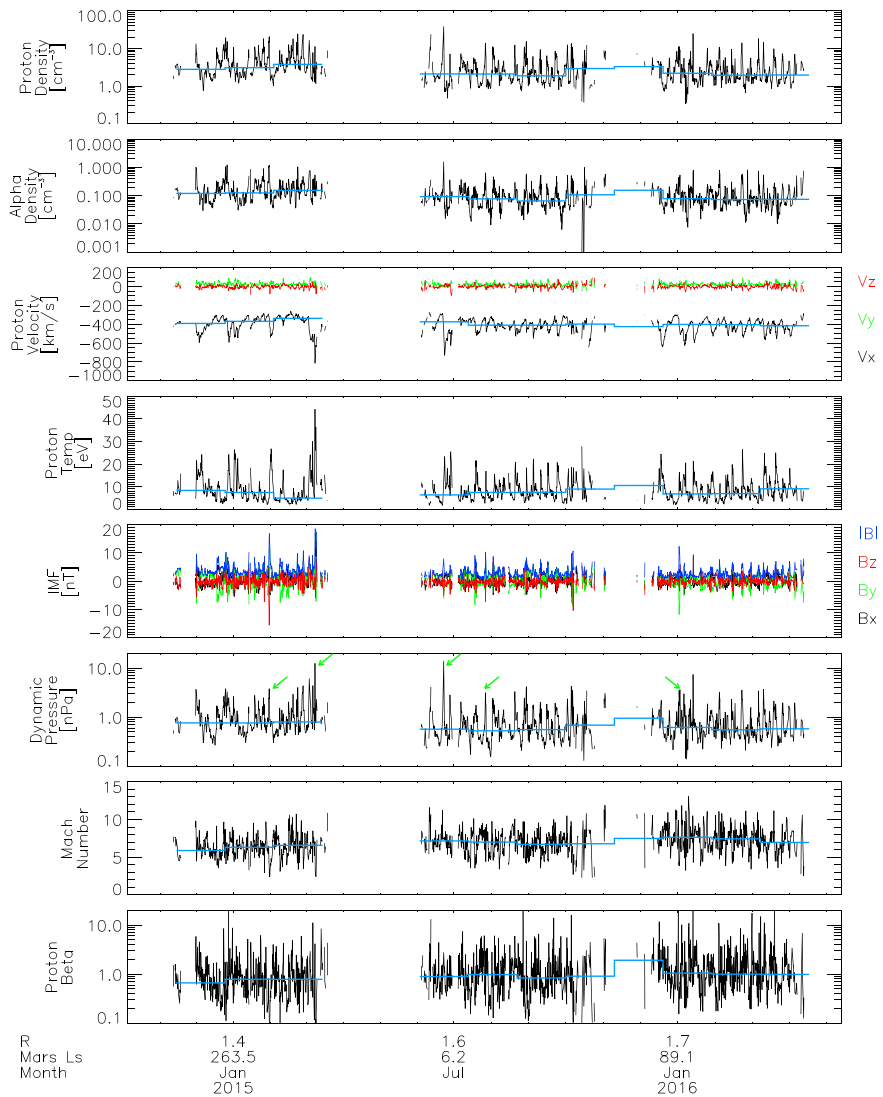


**Figure 4.** MAVEN solar wind proton and alpha density, proton velocity components, proton scalar temperature, interplanetary magnetic field (IMF) components and magnitudes, solar wind dynamic (ram) pressure, magnetosonic Mach number, and proton beta, constructed from SWIA and MAG measurements and averaged over the undisturbed upstream portion of each orbit. The light blue lines show median values for 40 day intervals. All vector quantities utilize MSO coordinates. Labels indicate the heliocentric distance of Mars in AU and Martian solar longitude  $L_5$ . Green arrows indicate events tentatively identified as coronal mass ejections (CMEs).

criterion deserves some explanation, since it utilizes mixed units, and relies on uncorrected onboard temperature moments. When accounting for the overestimate of temperature in the onboard moments due to alpha particle contamination, and converting to velocity units, this approximates the criterion  $v_{th}/|\mathbf{v}| < \sim 0.1$ . Assuming equal electron and ion temperatures, this amounts to requiring a sonic Mach number  $> \sim 6$ . This represents a conservative threshold, which will sometimes exclude high-temperature solar wind (such as that seen in the sheaths of coronal mass ejections, for instance). However, we found it necessary to keep this conservative threshold to reliably exclude magnetosheath data. We recognize that, as a result of our conservatism, we will undersample very hot solar wind conditions. We may also undersample periods with radial IMF as a result of the magnetic fluctuation criterion, which we require to eliminate foreshock contamination.

Utilizing this algorithm, we processed data from the entire mission to identify all periods during which MAVEN's orbit definitely passed through the upstream solar wind. We then computed averages of important solar wind quantities over the upstream portion of each MAVEN orbit and also over intervals with durations of

1/360 of the orbit (~45 s). We will use the latter data set in section 5. We show the orbit-averaged results in Figure 4, after postprocessing to remove a small percentage of orbits with magnetosonic Mach number  $< 2$  (due to false positive identifications of solar wind intervals), excessively high variations in density or velocity over a single orbit, and/or spacecraft attitudes that place the solar wind core out of the instrument FOV (during some communications orbits). The resulting data set covers ~60% of the MAVEN orbits, with most of the remainder consisting of orbits that did not extend outside of the bow shock (which naturally occurs during some time periods due to the orbit precession). All of the quantities shown in Figure 4 (with the exception of the IMF) represent the results of two-component moment computations that separate the contribution of protons and alphas. All ion quantities (other than the alpha density) utilize only the proton component from this computation. To compute the magnetosonic Mach number  $M_{MS} = v_{SW} / \sqrt{v_s^2 + v_A^2}$ , we assumed an electron temperature equal to the proton temperature and utilized the formula  $v_s = \sqrt{\frac{kT_e}{m} + \gamma \frac{kT_i}{m}}$  with a polytropic index  $\gamma = 5/3$ .

During the time period shown in Figure 4, MAVEN observed median solar wind densities of  $2\text{--}3 \text{ cm}^{-3}$ , with typical alpha abundances of 3–5%, median solar wind flow speeds of 350–450 km/s, median proton temperatures of 4–8 eV, median dynamic pressures of 0.6–0.8 nPa, median magnetosonic Mach numbers of 6–7, and median proton beta values of 0.7–1. We find an overall median antisunward velocity of  $-395 \text{ km/s}$ , with median off-axis components of 22.1 km/s and  $-0.4 \text{ km/s}$  in the Y and Z directions in Mars Solar Orbital (MSO) coordinates. The corresponding mean values are  $-408 \text{ km/s}$ , 23.7 km/s, and  $-0.9 \text{ km/s}$ . Given the average orbital speed of Mars around the Sun of 24.1 km/s, this suggests that SWIA resolves the off-axis flow velocity with an excellent accuracy and precision of  $\sim 1 \text{ km/s}$ . We find a moderate decrease in density and dynamic pressure and increase in Mach number and proton beta over the time period of Figure 4. These variations may include a solar cycle component but likely primarily reflect the changing heliocentric distance of Mars. The MAVEN upstream observations agree well with expectations from previous measurements at 1 AU and elsewhere in the heliosphere, taking into account the expected decrease in density and increase in Mach number and beta with heliocentric distance between Earth and Mars [Richardson *et al.*, 1996; Russell and Walker, 1995]. Direct comparisons with Mars Express and Earth-based solar wind measurements are ongoing and preliminary at this time.

In addition to a slow variation with heliocentric distance, most measured parameters vary by an order of magnitude or more around their median values, with structure primarily appearing at periods related to solar rotation, as expected given the normal rotation of solar wind sector boundaries and stream-stream interactions. Several moderate CMEs and one reasonably large CME [Jakosky *et al.*, 2015b] have impacted Mars during the MAVEN mission to date. These introduce significant excursions in IMF strength and dynamic pressure, beyond the normal level of variability in the nominal solar wind. The much more numerous CIRs introduce additional excursions that can prove comparable in some cases to those caused by CMEs. This variability provides a broad range of inputs, useful for parameterizing the structure of the Martian system and the atmospheric escape processes and loss rates.

### 3.2. Penetrating Proton Proxy Measurements of the Solar Wind

While the upstream data set of Figure 4 covers a substantial fraction of the mission, one would ideally like to have complete coverage of the solar wind. Fortunately, a portion of the solar wind charge exchanges with Martian exospheric constituents outside of the bow shock, converting it to energetic neutral atoms (ENAs) that do not feel electromagnetic fields and allowing them to penetrate to low altitudes in the atmosphere [Kallio *et al.*, 1997; Kallio and Barabash, 2001]. Below  $\sim 250 \text{ km}$ , some of these ENAs undergo electron stripping or electron attachment, converting them back to a charged form that we can measure [Halekas *et al.*, 2015c; Bougher *et al.*, 2015]. As described in Halekas *et al.* [2015c], we identify the  $\text{H}^+$  population resulting from this process and average the result over the altitude range 150–250 km to derive a proxy measurement of the solar wind. Energetic  $\text{O}^+$  pickup ions that precipitate into the atmosphere can contaminate this proxy. We filtered out their effects by removing inferred flow speeds above 700 km/s and retaining only orbits for which the inferred flow speed remains relatively constant, and the signal increases with decreasing altitude (characteristic of the collisional electron stripping of ENAs but opposite the expected trend for collisional neutralization of precipitating pickup ions). We also removed data from solar zenith angles (SZAs) greater than  $100^\circ$ , beyond which the penetrating protons typically do not have access to the spacecraft or experience

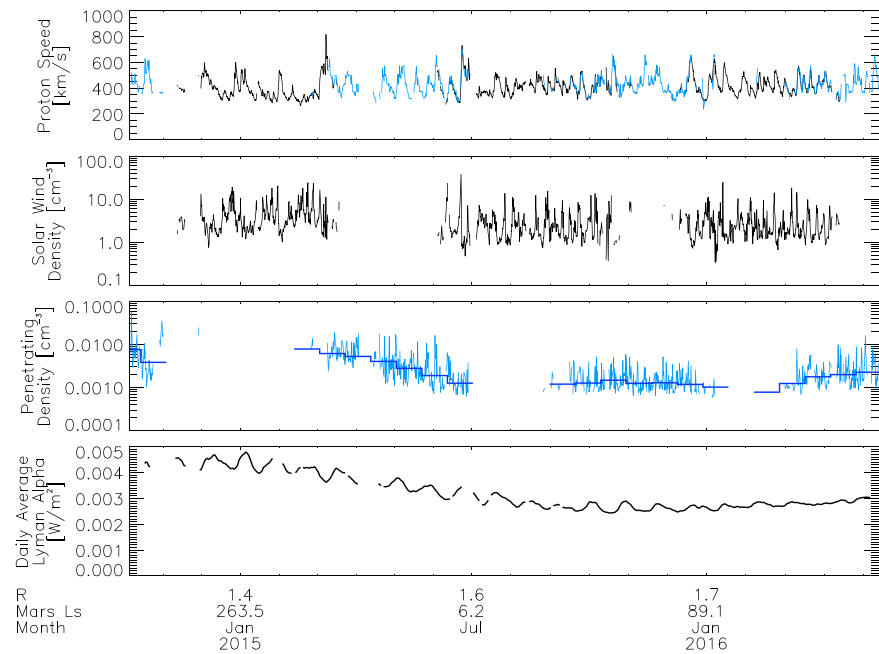


**Figure 5.** Comparison of upstream and penetrating proton data, with (first panel) the upstream solar wind (black) and penetrating proton (blue) speed, (second panel) the upstream solar wind density, (third panel) the penetrating proton density from the periapsis interval, and (fourth panel) the Lyman alpha photon flux from EUVM. The dark blue lines in Figure 5 (third panel) show median values for 20 day intervals. Labels indicate the heliocentric distance of Mars in AU and Martian solar longitude  $L_5$ .

too much absorption and scattering in the atmosphere to provide a reliable proxy. Finally, we employed a despiking algorithm to remove single-point outliers.

In Figure 5, we show the resulting flow speed and density measurements, along with the upstream solar wind flow speed and density and the directly measured EUV flux in the Lyman band from EUVM level 2 data [Eparvier *et al.*, 2015]. The proxy measurements fill in the gaps in the upstream data set, with some time periods of overlap during which the orbital geometry allows the measurement of both the upstream region and the penetrating population. In overlap periods, the inferred flow speed matches the upstream measurements, giving us confidence in the method. As discussed by Halekas *et al.* [2015c], by using the known energy dependence of the collisional cross sections, one can estimate the upstream density from the penetrating density and flow speed. However, this requires an assumption as to the total amount of solar wind charge exchange that occurs upstream of the bow shock.

As shown in Figure 5 (third panel), the charge exchange rate upstream of the shock must vary with time, since we observe a large decrease in the median penetrating proton density over the MAVEN mission, in addition to the expected solar wind variability. This decline most likely primarily reflects changes in the Martian exosphere, which we know to have a high degree of seasonal variability, thanks to spectroscopic observations [Chaffin *et al.*, 2014; Bhattacharyya *et al.*, 2015] and pickup ion measurements [Yamauchi *et al.*, 2015]. Given the results of Kallio *et al.* [1997], we expect that the SWIA observations should primarily reflect changes in the atomic hydrogen component of the corona, but if seasonal changes in the  $H_2$  and O exospheres occur, they could also play some role. In any case, SWIA observations indicate a remarkable level of seasonal variability in the exosphere, implying an order of magnitude variation in the column density that interacts with the solar wind outside of the bow shock during the time period surveyed. Other MAVEN observations of UV emission from the hydrogen corona, low-frequency waves seen upstream near the proton cyclotron frequency [Romanelli *et al.*, 2016], and pickup ions [Rahmati *et al.*, 2017] confirm a seasonal variation in the corona during the MAVEN mission. This variation closely tracks the EUV flux, which primarily varies with heliocentric distance over this time period (solar cycle effects may play a secondary role). However, our observations indicate an order of magnitude variation in

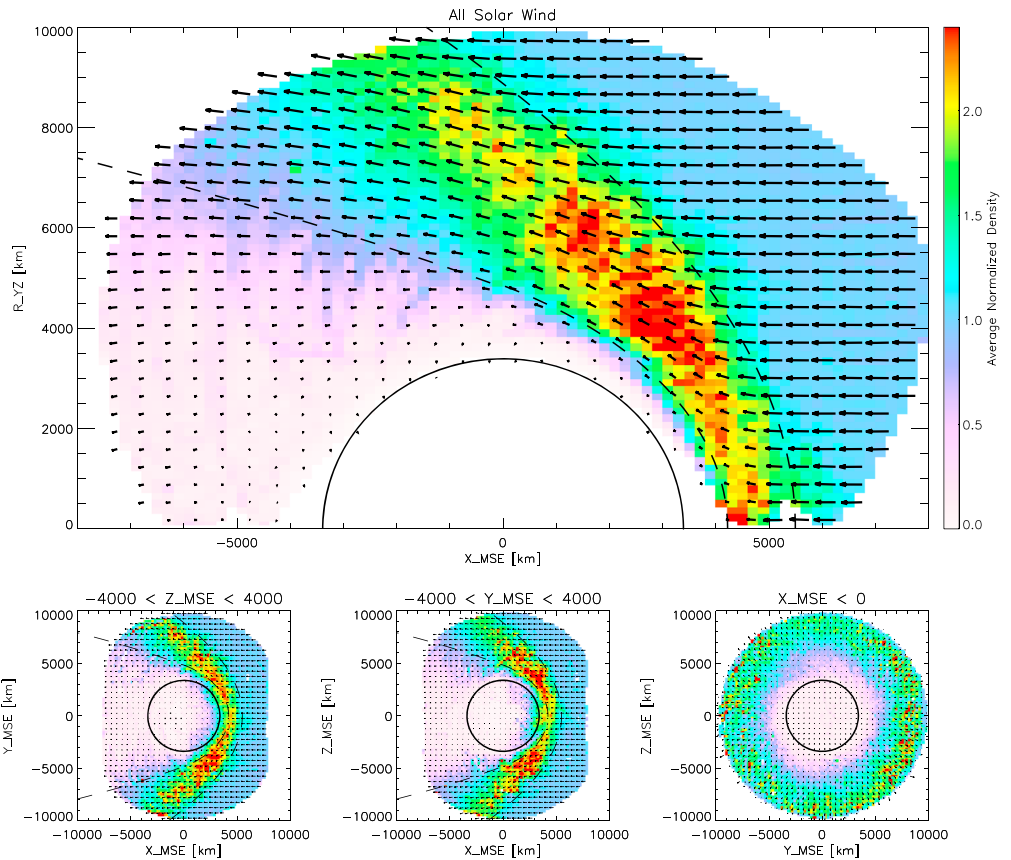


**Figure 6.** Average normalized density  $n/n_{sw}$  (in color) and projections of the velocity  $\mathbf{v}/|\mathbf{v}_{sw}|$  (vectors, normalized by the solar wind velocity on an orbit-by-orbit basis) from SWIA onboard moments from orbits during which MAVEN sampled the undisturbed upstream solar wind, organized in aberrated Mars Solar Electric (MSE) coordinates using SWIA and MAG data from the upstream interval. MSE coordinates orient the IMF in the X-Y plane with a positive Y component. (top) A spatial average of all data in a cylindrical projection. (bottom row) Three different projections of spatial averages of subsets, as shown in the panel legends. The dashed black curves show the nominal bow shock and magnetic pileup boundary (MPB) locations from *Trotignon et al.* [2006].

precipitating hydrogen during a time period over which the EUV varies by a factor of 2, implying a nonlinear dependence.

#### 4. Martian Magnetospheric Structure and Variability

##### 4.1. Average Martian Magnetospheric Structure

We constructed the upstream data sets described in section 3 to allow the MAVEN team and the greater scientific community to organize and parameterize the observed structure of the magnetosphere and the escape of atmospheric gases from the Martian system by the solar wind forcing terms. *Connerney et al.* [2015b], *Harada et al.* [2015], and *Dong et al.* [2015] showed examples of the use of early versions of the upstream data set to organize magnetic field and ion measurements in and around the Martian magnetosphere, demonstrating that the upstream drivers organize the MAVEN measurements well.

In this paper, we utilize the upstream drivers to organize the density and velocity measurements from SWIA and investigate the structure of the magnetosphere and its variability. We present all maps in the Mars Solar Electric (MSE) coordinate system, defined by the upstream IMF and the solar wind velocity such that its X axis lies antiparallel to the solar wind flow (including the aberration due to Mars' orbital motion), and the IMF lies in the X-Y plane with a positive Y component. In this coordinate system, the solar wind motional electric field always points along the +Z axis. Figure 6 shows spatially averaged maps of all SWIA onboard density and velocity moments returned from orbits with good upstream measurements,

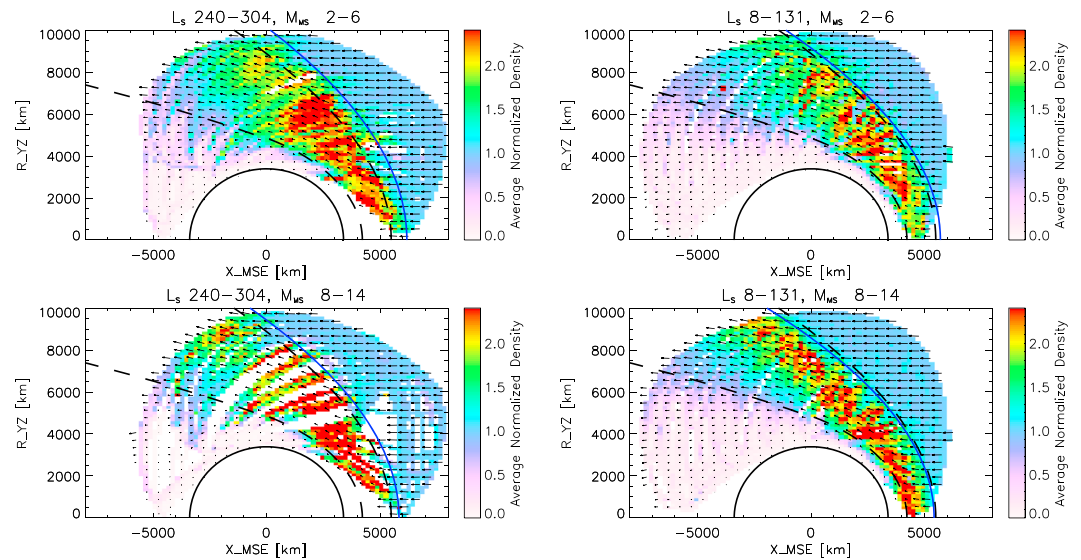


**Figure 7.** Four subsets of the observations from Figure 6 (top), from two different seasons, for two different solar wind magnetosonic Mach number ranges. The dashed black curves show the nominal bow shock and MPB locations from Trotignon *et al.* [2006]. The solid blue curves show the average bow shock locations for the four subsets from fits to conic sections with fixed focus and eccentricity but variable semilatus rectum.

in several different projections. Since the maps in Figure 6 average over all seasons and solar wind conditions, the boundary transitions appear more gradual than they would on any typical individual orbit. Nonetheless, the bow shock remains clearly apparent and corresponds to results from previous studies of Martian bow shock structure [Slavin *et al.*, 1991; Verigin *et al.*, 1993, 1999; Trotignon *et al.*, 2006; Vignes *et al.*, 2000, 2002].

These observations represent a new data set appropriate for the study of the upstream solar wind, bow shock, and magnetosheath. Note that one should not utilize the density and velocity moments shown here in a quantitative fashion inside the inner boundary of the sheath, where heavy ions dominate the composition, and significant fluxes below SWIA's 25 eV lower energy limit exist. Despite these limitations, the SWIA measurements do show a clear transition near the IMB/MPB location found by previous studies, particularly in the subsolar region of the magnetosphere. Our results compare favorably to similar statistical maps from Fraenz *et al.* [2006], though that previous work utilized mass-resolved measurements (and therefore had no contribution from heavy ions) but had a bias toward high velocities due to unmeasured protons below 500 eV.

Figure 6 (bottom row) demonstrates that the Martian bow shock and magnetosphere maintain a high degree of symmetry, at least in an average sense. Note that in MSE coordinates, one should not observe any Parker spiral asymmetry, since these coordinates mix different solar wind sectors. One might expect to observe asymmetries related to mass loading, but instead, the Martian bow shock and sheath appear remarkably symmetric in both the  $X$ - $Y$  and  $X$ - $Z$  planes. These results suggest that the location of the bow shock depends mostly on basic considerations of pressure balance and flow Mach number and that asymmetries due to mass loading have at most a secondary effect on its structure. We do find a few hints of asymmetries in the form of an apparent elongation of the tail cross section along the  $Z$  axis and a reduction of magnitude of the bow shock density jump in the  $\pm Z$  flank regions; however, given the limitations of SWIA observations in the heavy ion-dominated tail, further observations should confirm whether these represent robust characteristics of the magnetosphere.

#### 4.2. Seasonal and Solar Wind Effects on the Martian Magnetosphere

The structure of the bow shock and magnetosphere changes in response to seasonal and solar wind variations. To investigate this variability, in Figures 7 and 8 we show subsets of the data from two time periods, consisting of the first time interval with upstream coverage (from November 2014 to March 2015) and the

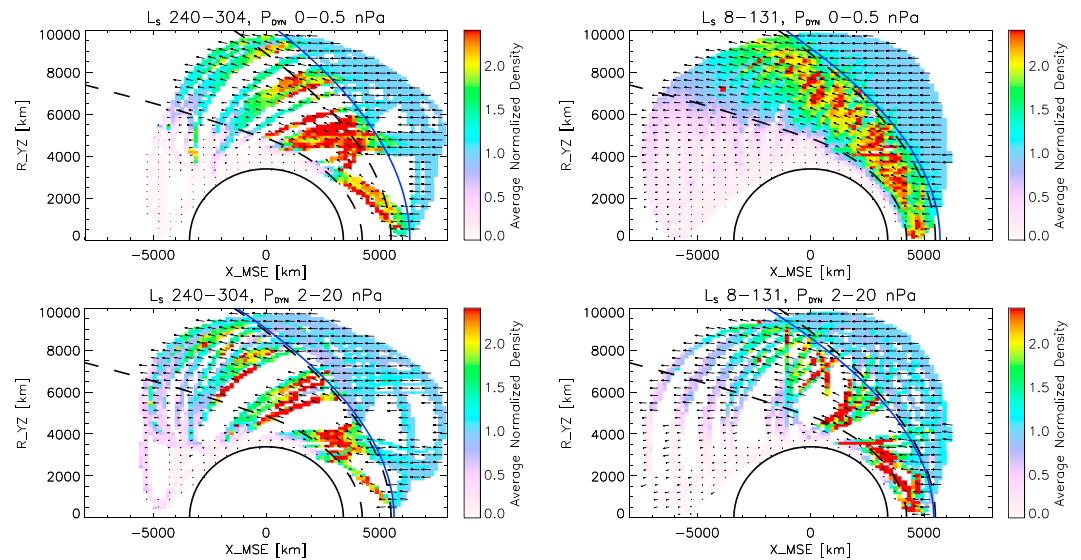


**Figure 8.** Four subsets of the observations from Figure 6 (top), from two different seasons, for two different solar wind dynamic pressure ranges. The dashed black curves show the nominal bow shock and MPB locations from *Trotignon et al.* [2006]. The solid blue curves show the average bow shock locations for the four subsets from fits to conic sections with fixed focus and eccentricity but variable semilatus rectum.

second two time intervals (June–October 2015 and December 2015 to May 2016) combined. As shown in Figure 5, during the first time period, with Mars solar longitude  $L_S$  of 240–304 (southern summer, including perihelion and the typical “dust storm season” of Mars), the MAVEN EUVM observed Lyman alpha fluxes of  $0.0035\text{--}0.005\text{ W/m}^2$ . During the second time period, with  $L_S$  of 8–131 (southern fall and winter, including aphelion), EUVM measured Lyman alpha values of  $0.002\text{--}0.0035\text{ W/m}^2$ . In Figure 7, we further subselect data with low and high solar wind magnetosonic Mach number  $M_{MS}$ . In Figure 8, we further subselect data with low and high solar wind dynamic pressure  $P_{DYN}$ .

The results of Figures 7 and 8 clearly show that both the Mars season and the solar wind affect the extent of the Martian bow shock and the structure of the magnetosphere. In agreement with previous results from MEX, increased EUV results in the bow shock moving outward, while increased dynamic pressure and Mach number decrease the extent of the bow shock [Edberg *et al.*, 2009, 2010a]. We quantified the effects of these parameters by numerically fitting the 2-D cylindrical gridded array of density observations to an average conic section model, using the approximation of a constant density jump (a step function) across the portion of the shock covered by the MAVEN observations, and fitting to measurements with density greater than or equal to the undisturbed solar wind (thereby excluding data from within the MPB/IMB). We followed the Edberg *et al.* [2009] technique and held the focus  $x_0$  and eccentricity  $\epsilon$  constant (with values of  $0.6 R_M$  and 1.0) while varying the shock density jump and the semilatus rectum  $L$ . While one could fit for all four parameters with a 2-D array of data, the conic section parameters proved highly colinear, especially given the limited extent of the MAVEN coverage at large distances on the flanks. Using this constrained fitting procedure, we found  $L$  values of 2.46 for high EUV and low  $M_{MS}$ , 2.26 for high EUV and high  $M_{MS}$ , 2.17 for low EUV and low  $M_{MS}$ , and 2.01 for low EUV and high  $M_{MS}$ . Meanwhile, we found  $L$  values of 2.54 for high EUV and low  $P_{DYN}$ , 2.13 for high EUV and high  $P_{DYN}$ , 2.17 for low EUV and low  $P_{DYN}$ , and 2.01 for low EUV and high  $P_{DYN}$ . Thus, even when averaging over large numbers of orbits taking place under a range of conditions, the combined variability in  $L$  amounts to over half a Martian radius, translating to a variation in subsolar position of the shock of  $\sim 900\text{ km}$  above the surface, a significant fraction of the nominal standoff distance of  $\sim 2100\text{ km}$ . We will see that on individual orbits even larger variations occur.

We find a weaker than expected dependence of the shock density jump on Mach number. For low EUV conditions, we do find a stronger shock jump at high Mach numbers, especially on the flanks. However, for high EUV conditions, we find little obvious difference between the strength of the low and high Mach number shock. The high Mach number range has less coverage for this time period, so we may simply lack statistics.

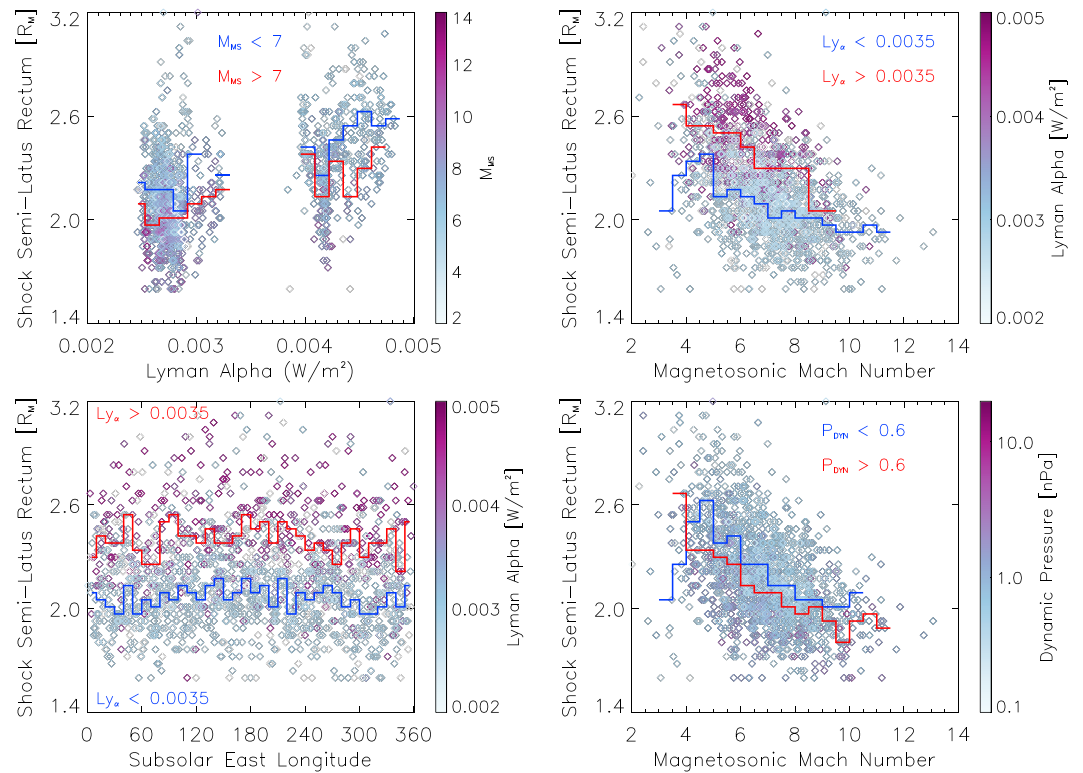


**Figure 9.** Semilatus rectum ( $L$ ) values for conic section fits (with fixed focus and eccentricity) to SWIA density profiles from orbits during which MAVEN sampled the undisturbed upstream solar wind. (top left)  $L$  as a function of Lyman alpha flux ( $Ly_{\alpha}$ ) from EUVM, with one point per orbit, with colors indicating the solar wind magnetosonic Mach number  $M_{MS}$ , along with median values for two Mach number ranges (blue and red curves). (top right)  $L$  as a function of  $M_{MS}$ , with colors indicating  $Ly_{\alpha}$ , along with median values for two  $Ly_{\alpha}$  ranges. (bottom left)  $L$  as a function of subsolar geographic longitude, with colors indicating  $Ly_{\alpha}$ , along with median values for two  $Ly_{\alpha}$  ranges. (bottom right)  $L$  as a function of  $M_{MS}$ , with colors indicating solar wind dynamic pressure, along with median values for two dynamic pressure ranges.

SWIA observations can miss some of the density in the sheath, but we have no reason to suspect a systematic FOV coverage effect related to Mach number. Alternatively, some other confounding factor may play a role.

High Mach number shocks at Mars may differ to some degree from the ideal case. Observations of the Earth's bow shock suggest that for quasi-perpendicular shocks the ramp and overshoot scale with the trapped ion gyroradius, many ion inertial lengths for high Mach number solar wind [Bale et al., 2003]. Similar scaling at Mars, consistent with Phobos-2 observations [Tatallyay et al., 1997], would imply ramp and overshoot scales as large as ~500 km for the high Mach number range, only a factor of 2 smaller than the expected thickness of the subsolar sheath. The observations in Figures 2 and 3 appear consistent with this expectation. The individual observations also show significant oscillations in the density that may lead to a general smearing out of the largest shock jump in the spatial averages shown in Figures 6–9. Finally, cold ions produced from the hydrogen exosphere may play a significant role near the bow shock at Mars [Dubinin et al., 1993b], further complicating the picture.

We find it interesting to note the competing effects of heliospheric distance on the Martian system. Increasing heliospheric distance reduces the EUV input to the upper atmosphere, reducing the shock scale and “deflating” the Martian magnetosphere, all other factors being equal. Increasing heliospheric distance also tends to increase the Mach number of the flow [Russell and Walker, 1995], which has a similar effect. However, the increase in heliocentric distance also reduces the average solar wind density and ram pressure, which has the effect of increasing the size of the magnetosphere. Thus, the weaker solar wind flow at aphelion in part masks the effects of the weaker solar EUV. While we lack a long enough baseline of observations to make definitive statements about solar cycle variations, one might expect a similar interplay between competing solar energy inputs to occur over the solar cycle. This masking effect may have led previous authors to

suggest that the mean shock surface does not depend on solar cycle [Vignes *et al.*, 2000], a conclusion which we should revisit once we have sufficient data. Similar considerations may also result in competing effects on the escape of ions from the Martian system.

#### 4.3. Variability in the Bow Shock Location at Mars

To further investigate the role of seasonal and solar wind drivers on the Martian bow shock, we considered orbit-to-orbit variability. We utilized exactly the same fitting procedure as above, but with individual orbits of data (instead of ensembles) gridded in the same cylindrical projection. Note that in the case of multiple shock crossings, this procedure will typically return an average shock location. For this study, we used density moments computed on the ground from the Coarse 3-D distribution rather than the onboard moments, in order to eliminate any potential issues with mode changes near the bow shock. We show the resulting shock scale parameter  $L$  as a function of Mach number, EUV, dynamic pressure, and subsolar longitude in Figure 9. For individual orbits, as one would expect, we find a much higher degree of variability than we did for binned groups of data in the previous section. For individual orbits we find  $L$  values ranging from 1.6 to 3.2  $R_M$ , corresponding to subsolar standoff distances of 0.4–1.2  $R_M$  from the surface of Mars, a variation of ~2700 km in the standoff distance, a remarkable range of variability in the Martian bow shock location.

In agreement with the MEX results from Edberg *et al.* [2009, 2010a], Mach number and EUV represent the two most significant controlling factors (as expected from basic principles). To compare directly to previous results, one can compute the terminator position of the bow shock  $R_T = L\sqrt{1 + 2x_o/L}$ , which varies over a range of 2.01–3.75  $R_M$  for the MAVEN observations. These results appear somewhat higher than those found by Edberg *et al.* [2009, 2010a] studies, but that previous study utilized data from 2004 to 2009, a period of very weak solar activity spanning solar minimum. The conditions they considered more closely correspond to those encountered by MAVEN in June 2015 to April 2016, during which EUVM observed Lyman alpha fluxes of 0.002–0.0035 W/m<sup>2</sup>. For that time period (left-hand side of top left panel and blue median curves in top right and bottom left panels of Figure 9), our observations closely match those from the previous study, with most  $L$  values between 1.6 and 2.6  $R_M$ , corresponding to  $R_T$  values of 2.1–3.1  $R_M$ , very much in agreement with the previous results.

In addition to the Mach number and EUV dependence, we find that even when holding Mach number constant, dynamic pressure plays a role in determining the shock position, indicating that the solar wind can compress the ionospheric obstacle to some degree (in agreement with Edberg *et al.* [2009]). Finally, as shown in Figure 9 (bottom left), a weak dependence on subsolar longitude exists over all EUV ranges, most likely due to the effects of crustal fields in increasing the obstacle scale, confirming the weak dependence found by Edberg *et al.* [2008, 2009].

## 5. The Foreshock and Upstream Region of Mars

### 5.1. Mass Loading Upstream From the Martian Bow Shock

Induced magnetospheres result from the interaction of the solar wind with heavy ions produced from atmospheres and/or exospheres, which involves at least two different mechanisms. First, induced currents in the ionosphere oppose the penetration of the solar wind magnetic field, resulting in draping and pileup of the IMF around the ionosphere (balancing the solar wind dynamic pressure with compressed field and plasma and then balancing that with ionospheric thermal pressure). Second, mass loading by heavy ions [Szego *et al.*, 2000] slows the solar wind flow, also leading to draping and pileup of the IMF around the ionosphere. Both of these mechanisms can result in the formation of a bow shock and magnetosphere. At comets, which have weak gravity and extended exospheres (comae), mass loading dominates [Ip and Axford, 1982]. Active releases of gas also point to the importance of mass-loading effects for smaller-scale obstacles [Haerendel *et al.*, 1986]. Recently, McComas *et al.* [2016] suggested that Pluto also has a solar wind interaction governed primarily by mass loading.

On the other hand, Venus and Mars are expected to have an interaction governed by ionospheric thermal pressure and conductivity, with mass loading only playing a role very close to the planet and in the magnetotail [Luhmann, 1995]. Though Phobos-2 observations initially suggested large solar wind decelerations upstream from Mars [Verigin *et al.*, 1991; Kotova *et al.*, 1997], Dubinin *et al.* [2000] demonstrated that those

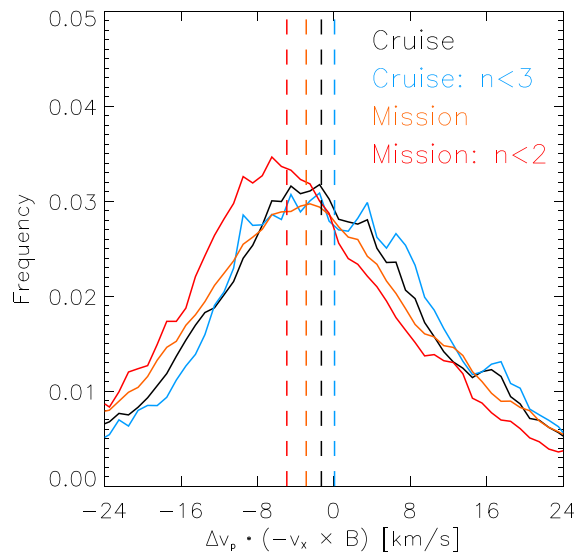


**Figure 10.** Frequency distributions of the component of the residual off-axis velocity  $\Delta v_p$  parallel to the nonradial component of the motional electric field (i.e., the dot product of  $\Delta v_p$  with a unit vector along  $-\mathbf{v}_x \times \mathbf{B}$ ). We define  $\Delta v_p$  as the difference between the SWIA onboard velocity moment and the velocity corresponding to a purely radial flow outward from the Sun plus the aberration due to the lateral motion of the MAVEN spacecraft around the Sun. The black and blue curves show frequency distributions from cruise (March–April 2014) for all measurements and for a subset with low solar wind density. The orange and red curves show frequency distributions from the prime mission (October 2014 to May 2016) for all measurements in the upstream solar wind and for a subset with low solar wind density. All calculations for cruise and mission data utilize measurements averaged over 45 s intervals. Vertical dashed lines show the four corresponding median values.

heavy ions). At comets, this lateral deflection can prove quite important, leading to angular deflections of the solar wind of 50° or more close to the nucleus [Goldstein et al., 2015; Nilsson et al., 2015; Behar et al., 2016].

From a single spacecraft with a small orbit like that of MAVEN, detecting weak signatures of upstream mass loading from the slowdown of the flow proves difficult if not impossible, at least without some a priori knowledge of the unmodified flow speed. However, MAVEN can utilize the highly sensitive SWIA measurements of off-axis velocity components to search for a weak mass-loading signature upstream from Mars. To accomplish this, we investigated the deviations from the expected average flow direction given by the vector addition of radial outflow with the orbital motion of Mars around the Sun. In Figure 10 we show statistical distributions of the component along the  $-\mathbf{v}_x \times \mathbf{B}$  nonradial motional electric field of the lateral deviation  $\Delta v_p$  from the expected mean flow velocity, using the 45 s averaged upstream data set described in section 3.1. To calculate this quantity, we utilized data taken in Fine mode, much less subject to contamination from nonsolar wind sources such as reflected ions from the shock, given the constrained region of phase space covered. In the absence of mass loading, the distribution of this quantity should have its center at or near zero, while the presence of mass loading should deflect the solar wind opposite to the direction of the unperturbed motional electric field, shifting the distribution toward more negative values. Indeed, distributions of lateral velocities obtained during cruise, though they have a slightly skewed form, have a median within ~1 km/s of zero for all cruise data and for low-density solar wind data. On the other hand, in orbit around Mars, the distribution for all upstream observations has a median of -2.9 km/s, while the distribution for low-density solar wind (more susceptible to mass loading) has a median of -4.9 km/s. The Student's *t* test and the Mann-Whitney *U* test [Corder and Foreman, 2014] indicate that the distributions obtained during the prime mission differ from those from cruise to a high degree of significance (the chance of the distributions having the same mean or median is zero to the accuracy of floating point arithmetic). These results therefore suggest that weak mass loading does occur upstream from Mars.

features only occurred in the fore-shock and suggested that rather than mass loading, large-amplitude Alfvén waves played the primary role in generating the observed signatures.

Mass loading slows the solar wind flow, in order to conserve momentum in the flow direction. However, on smaller scales, it also deflects the solar wind laterally. Newly born pickup ions experience a force along the motional electric field and initially accelerate directly along the electric field (later they bend around the magnetic field and follow cycloidal trajectories—however, the scale of the cycloid can exceed the size of the Martian system for heavy ions). This lateral acceleration of heavy ions extracts momentum from the solar wind, and as a result the solar wind must deflect in the opposite direction from the original motional electric field to conserve momentum (as an alternative way to see this, consider the motional electric field seen by the solar wind ions in their rest frame as the electron fluid and the embedded magnetic field slow down to balance the addition of charge by

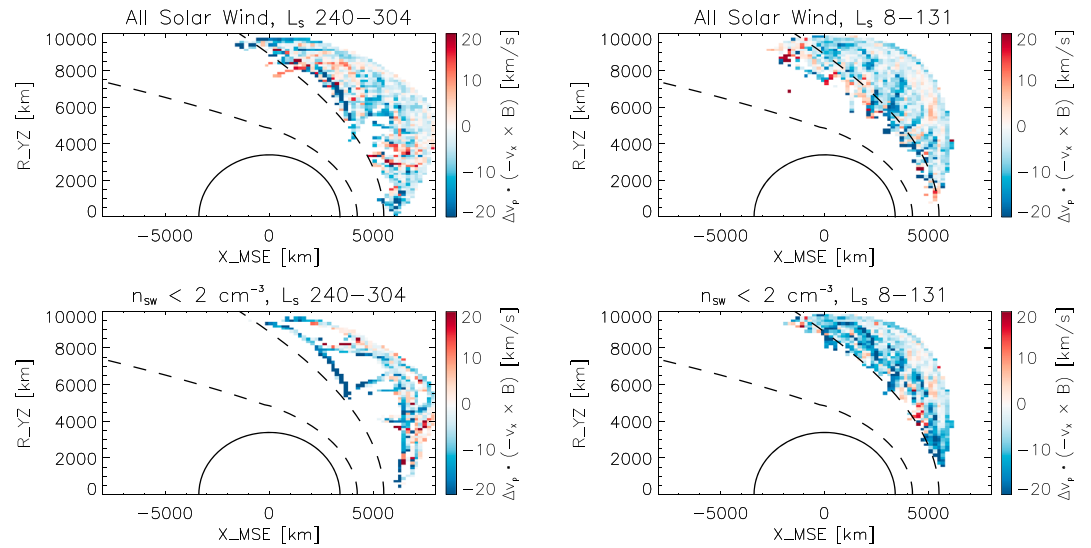


**Figure 11.** Spatial averages of the off-axis residual velocity measurements made upstream from the bow shock during the prime mission (same data as the orange and red frequency distributions from Figure 10), in a cylindrical projection, separated into two different seasons. The dashed black curves show the nominal bow shock and MPB locations from Trotignon et al. [2006].

Figure 11 shows averaged spatial distributions of the quantity described in the preceding paragraph. For the data set consisting of all the upstream measurements, we find no clear organization with distance upstream from the bow shock. We also found no organization by location within or outside of the foreshock (not shown), somewhat surprising given previous results showing apparent mass loading in the foreshock [Dubinin et al., 2000]. For low-density solar wind observations, we do find a weak but suggestive trend toward more negative values closer to the bow shock, consistent with the expected mass-loading signature, which should increase with the column depth of neutral gas encountered by the solar wind in the region upstream from the shock. The observations do not clearly show any seasonal dependence, which one might expect to find given the apparent variability of the corona around Mars (see section 3.2). However, the high-EUV interval has relatively few observations with low solar wind density, making it difficult to draw statistically robust conclusions about the seasonal variability of mass loading.

We can roughly estimate the planetary ion content upstream from the shock by considering the conservation of momentum in the direction perpendicular to the initial flow. To first order,  $n_p m_p \frac{dv_z}{dt} = q n_i v_x B_y$  (written in terms of the proton velocity components and the solar wind proton and planetary ion densities  $n_p$  and  $n_i$ ), determined by balancing the change in momentum of the solar wind and planetary ions in the MSE Z direction. Integrating this equation over the streamline upstream of the bow shock position  $r_0$ , we find that  $\Delta v_z = -\frac{q B_y}{n_p m_p} \int_{r_0}^{\infty} n_i dx$ , which indicates that the lateral velocity change scales with the proton cyclotron frequency and with the ratio between the column depth of planetary ions that the solar wind interacts with and the solar wind proton density. Taking a median lateral velocity change of  $-5 \text{ km/s}$  for the low-density case, a typical perpendicular IMF component of  $2 \text{ nT}$ , and a solar wind proton density of  $1.5 \text{ cm}^{-3}$ , this calculation would imply a planetary ion column depth upstream from the bow shock of  $\sim 4 \times 10^6 \text{ cm}^{-2}$ . For an exponential distribution with a scale height on the order of a Martian radius, this would correspond to a planetary ion density near the bow shock of  $\sim 0.01 \text{ cm}^{-3}$  or about 0.7% of the solar wind density. Even this very small value exceeds the  $2 \times 10^{-3} \text{ cm}^{-3}$  value Dubinin et al. [2006b] measured for pickup  $\text{H}^+$  density near the bow shock, so SWIA observations may indicate that other planetary ion species such as  $\text{H}_2^+$  and  $\text{O}^+$  also play a role in mass-loading the flow near the bow shock. In any case, MAVEN results indicate that planetary ions do not strongly mass load the flow outside of the bow shock and therefore play at most a minor role upstream from the bow shock of Mars.

## 5.2. Alfvén Waves Upstream From the Martian Bow Shock

Several factors contribute to the broad distribution of off-axis velocities seen in Figure 10, all of which make positive identification of upstream mass loading more difficult. CMEs and stream interactions such as CIRs can lead to transient periods of nonradial flow. In addition, Alfvén waves with a wide range of wavelengths pervade the upstream medium, creating ubiquitous correlated fluctuations in magnetic field and velocity that can reach amplitudes of several nanotesla and several tens of km/s [Belcher and Davis, 1971]. This solar wind Alfvénic turbulence may have implications for the Martian system. At the Earth, solar wind Alfvén waves can affect both the ionosphere and the neutral thermosphere [Prikryl et al., 2005]. Similarly, wave energy may propagate from the solar wind into the Martian magnetosphere, potentially providing an energy source to heat ionospheric particles to escape velocity or beyond [Ergun et al., 2006]. In addition, turbulent fluctuations in the upstream magnetic field could lead to reconnection in the magnetosheath and/or magnetosphere, as draped IMF field lines with different orientations interact.

To investigate the Alfvén wave input to the Martian system, we utilized the 45 s average upstream data set described in section 3.1. This averaging effectively suppresses contributions from frequencies near the proton cyclotron frequency (stimulated locally in the Martian environment [Brain et al., 2002; Espley et al., 2004; Mazelle et al., 2004; Ruhunusiri et al., 2015]) while retaining the lower frequency components more likely of solar wind origin. To calculate the fluctuation amplitudes at each time point, we computed the difference from a running mean value from the surrounding half-hour window. We utilized the vector fluctuations of the magnetic field  $\delta\mathbf{B}$  and of the velocity  $\delta\mathbf{v}$ , with the former converted to velocity units by multiplying by  $v_A/B_0 = 1/\sqrt{\mu_0\rho}$ . From these fluctuations we computed several quantities of interest, including the normalized cross helicity  $\sigma_c = 2\delta\mathbf{v} \cdot \delta\mathbf{B}/(\delta\mathbf{v}^2 + \delta\mathbf{B}^2)$ , the normalized residual energy  $\sigma_r = (\delta\mathbf{v}^2 - \delta\mathbf{B}^2)/(\delta\mathbf{v}^2 + \delta\mathbf{B}^2)$ , and the Alfvén ratio  $r_A = \delta\mathbf{v}^2/\delta\mathbf{B}^2$ . The cross helicity provides a measure of the correlation between velocity and magnetic field fluctuations, with a value of  $\pm 1$  indicating the propagation of a pure Alfvén wave antiparallel or parallel to the magnetic field direction. The residual energy and the Alfvén ratio provide two complementary measures of the balance between velocity and magnetic field fluctuations.

The prevalence of Alfvén waves in the solar wind varies with heliocentric distance and latitude [Bavassano et al., 1998; Breech et al., 2005], with the solar cycle [Perri and Balogh, 2010] and with solar wind parameters [Roberts et al., 1987]. Typically, in the solar wind, outward propagating Alfvén waves dominate, leading to negative cross helicities for outward IMF sectors and positive cross helicities for inward IMF sectors [Roberts et al., 1987]. Negative values of residual energy typically predominate (corresponding to  $r_A < 1$ ), indicating the dominance of magnetic fluctuations over velocity fluctuations [Roberts et al., 1987; Bavassano et al., 1998]. This imbalance may result from the presence of convected magnetic structures [Tu and Marsch, 1991] and/or the effects of anisotropic pressure and relative streaming on the Alfvén velocity [Bavassano et al., 1998; Goldstein et al., 1995].

Figure 12 shows the Alfvén wave properties observed in the upstream medium by MAVEN during the prime mission to date, with the values from cruise shown for reference. We find a predominance of outward-propagating (with respect to the Sun) Alfvén waves throughout the mission, with more negative cross helicities for  $+B_y/-B_x$  IMF sectors and more positive cross helicities for  $-B_y/+B_x$  sectors. However, we find a somewhat higher fraction of outward propagating waves during the early portions of the MAVEN mission (comparable to or higher than the value observed during cruise) and generally lower values later in the mission. The reason for this decrease remains unclear; however, the increase in heliospheric distance and the observed increase in the number of stream-stream interactions (see Figure 4) could both reduce the cross helicity [Roberts et al., 1987]. Meanwhile, magnetic fluctuations dominate over velocity fluctuations throughout the mission, with relatively constant median normalized residual energies of  $-0.5$  and median Alfvén ratios of  $0.33$ , virtually identical to the values from cruise, and well within the range typically seen in the solar wind [Bruno and Carbone, 2005]. The proportion of energy in velocity fluctuations increases at the beginning and end of each solar wind interval, suggesting an increase in velocity fluctuations closer to the bow shock. This may in part result from the mass-loading effects discussed in section 5.2, which would lead to velocity perturbations, but not magnetic field perturbations.

To further investigate how the presence of Mars affects the properties of solar wind Alfvén waves, we consider spatial distributions of the Alfvén wave parameters. To search for asymmetries in the cross helicity in

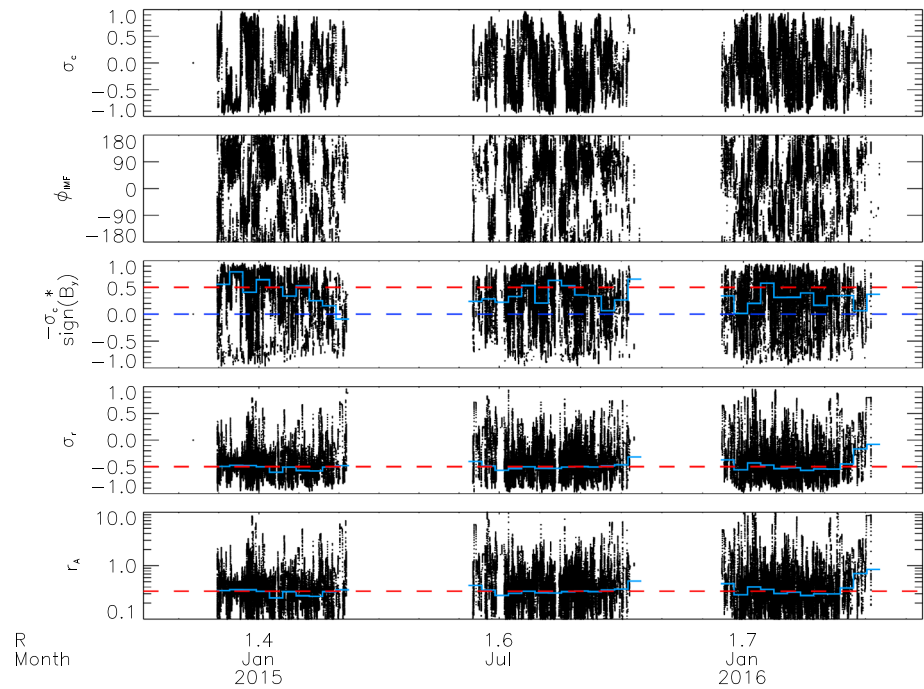


**Figure 12.** The normalized cross helicity, azimuthal angle of the IMF in the ecliptic  $\tan^{-1}(B_y/B_x)$ , negative of the normalized cross helicity multiplied by the sign of the IMF  $B_y$  (Alfvén waves propagating out from the Sun should have a positive value of this quantity), normalized residual energy, and Alfvén ratio. The black points show values computed from SWIA onboard moments and MAG measurements from the upstream solar wind taken during the prime mission (October 2014 to May 2016), the dashed red lines show median values from cruise (March–May 2014), and the dashed blue line in the third panel shows the zero level. All calculations for cruise and mission data utilize measurements averaged over 45 s intervals, with fluctuation amplitudes computed by subtracting the mean values from the surrounding half-hour window. The light blue lines in the third to fifth panels show median values for 10 day intervals. Text labels indicate the heliocentric distance of Mars in AU.

both toward and away IMF sectors, and for different seasons, we separate the data into four subsets based on the IMF  $B_y$  component and the time range, and show the results in Figure 13 (top and middle rows). We find that the coherence of the observed Alfvén waves decreases in the quasi-parallel foreshock ( $-Y$  side of top row and  $+Y$  side of middle row), consistent with the effects of the large-amplitude compressive fluctuations present in that region. Other than this foreshock effect, we find no clear spatial variation in the cross helicity, indicating that the temporal variability identified in Figure 12 does not result from differences in orbital geometry. Instead, the temporal decrease in cross helicity appears to affect all upstream regions sampled by MAVEN equally, providing supporting evidence that the observed decline represents a real change in the solar wind input rather than an effect driven by the presence of Mars. This change in the turbulent properties of the driving solar wind between perihelion and aphelion may further complicate the separation of seasonal and solar wind effects, adding to the confusion due to the competing effects of the changes in EUV and solar wind with heliocentric distance discussed in section 4.2.

As seen in Figure 13 (bottom row), energy is preferentially transferred to velocity fluctuations near the bow shock (as we also concluded from the time series data in Figure 12). This indicates that the presence of Mars does perturb the upstream region to some degree, even in the relatively pristine solar wind identified by the algorithm discussed in section 3.1. Though not shown in the figure, this transfer of energy to velocity fluctuations occurs to roughly the same degree near both the quasi-parallel and quasi-perpendicular portions of the bow shock, and for all time periods studied. This suggests that this transfer of energy does not stem from compressional fluctuations or other foreshock effects and instead potentially implicates the effects of mass loading. Alternatively, it could result from the transport of energy from larger to smaller scales due to increased dissipation by wave-particle interactions near the shock. However, it remains unclear why this would lead to an increase in the proportion of energy in velocity fluctuations as compared to magnetic fluctuations.

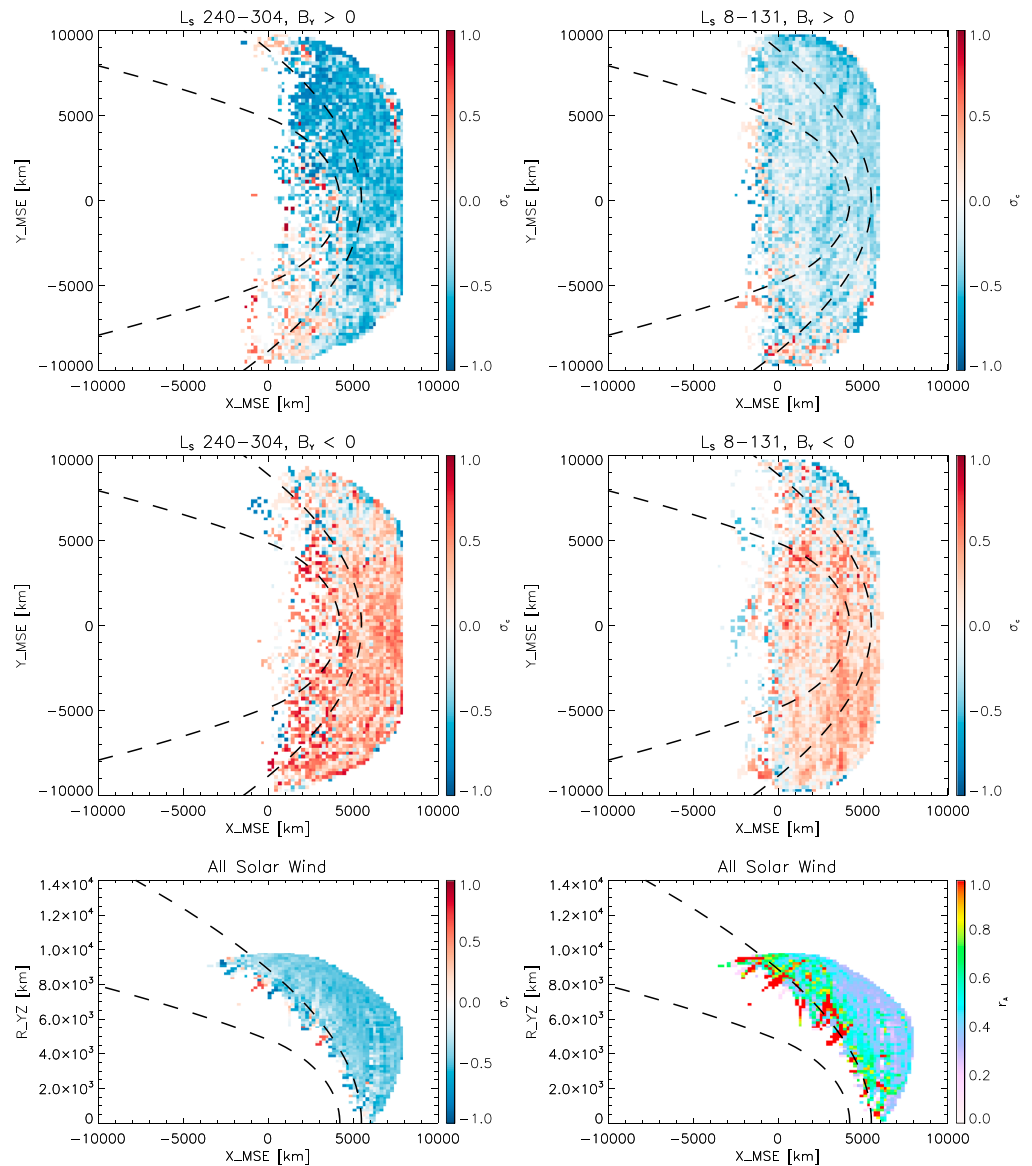


**Figure 13.** (top and middle rows) Spatial averages of the normalized cross helicity computed from measurements in the upstream solar wind during two different seasons, for time periods with positive and negative IMF  $B_y$  (in MSO coordinates), projected to the  $X$ - $Y$  plane of the aberrated MSE coordinate system. Assuming Parker spiral IMF ( $+B_y/-B_x$  or  $-B_y/+B_x$ ) geometry, Alfvén waves propagating out from the Sun should have negative cross helicity for  $+B_y$  and positive for  $-B_y$ . The quasi-parallel foreshock should lie on the  $-Y_{MSE}$  side for  $+B_y$  and on the  $+Y_{MSE}$  side for  $-B_y$ . (bottom row) The normalized residual energy and Alfvén ratio for all solar wind measurements from the prime mission, in a cylindrical projection. The dashed black curves on all panels show the nominal bow shock and MPB locations from Trotignon *et al.* [2006].

### 5.3. Upstream Events at Mars

On most orbits that sample the region upstream from the Martian bow shock, MAVEN observes only low-frequency waves, the omnipresent Alfvénic turbulence of the solar wind, and the faint signatures of mass loading discussed above. However, at some times, the presence of the Martian obstacle leads to much larger perturbations to the upstream plasma flow. These include both isolated events and groups of repeated quasi-periodic events, with both types of events capable of driving compressional changes in the solar wind density and magnetic field strength of over 100%, as well as decelerations and/or deflections of the solar wind flow by hundreds of km/s. In this penultimate portion of the paper, we investigate the characteristics of these upstream events and the conditions under which they occur.

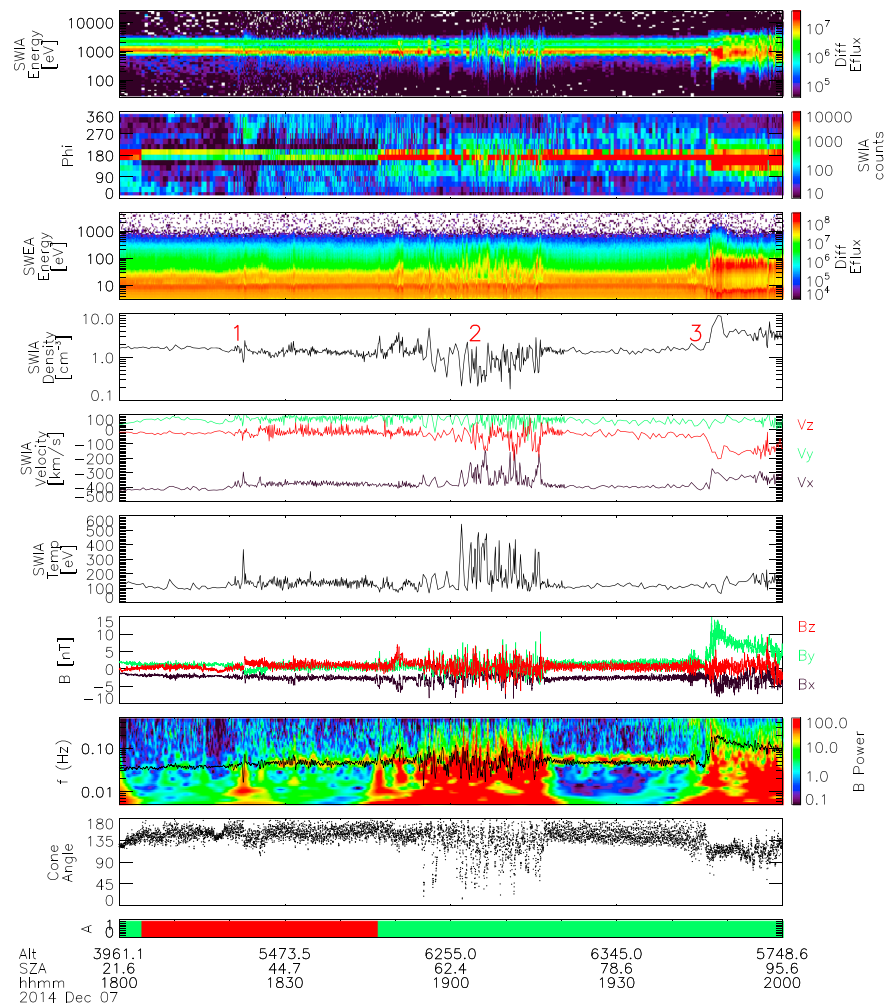


**Figure 14.** MAVEN measurements near apoapsis from an orbit with several upstream events. The panels show SWIA Coarse energy and instrument phi angle spectra, SWEA electron energy spectra, density, velocity, and scalar temperature computed from SWIA Coarse distributions, magnetic field components, power spectrum of magnetic field fluctuations (with proton cyclotron frequency in black), and the cone angle  $\cos^{-1}(B_x/|B|)$  from MAG measurements. Ion and electron energy spectra utilize units of  $\text{eV}/(\text{eV cm}^2 \text{ s sr})$ , and vector quantities utilize the MSO coordinate system. The color bar indicates the attenuator status (green = open, red = closed), and text labels indicate the spacecraft altitude in kilometers and solar zenith angle. The “1” on the density panel marks an isolated upstream event, the “2” marks a group of repeated events, and the “3” marks the bow shock.

A wide variety of phenomena have been observed upstream from the bow shocks of the terrestrial planets, including a host of ULF waves near the proton cyclotron frequency [Russell and Hoppe, 1983; Eastwood et al., 2005]. Reflected protons from the shock can drive these waves at both the Earth and Mars, and newly born ions from the extended exosphere can also drive waves at similar frequencies at Mars [Russell et al., 1990; Mazelle et al., 2004]. Given sufficient nonsolar wind ion fluxes and appropriate IMF geometry (frequently found in the quasi-parallel foreshock), ion-ion instabilities [Gary, 1991] can steepen and become nonlinear, forming structures such as foreshock cavitons [Blanco-Cano et al., 2009], foreshock cavities [Sibeck et al., 2002; Øieroset et al., 2001], the foreshock compressional boundary (FCB) [Omididi et al., 2009], and Short Large Amplitude Magnetic Structures (SLAMS) [Thomsen et al., 1990; Schwartz and Burgess, 1991; Schwartz et al., 1992; Burgess et al., 2005]. These structures typically have heated and partially isotropized plasma in their interior with slower (or even backstreaming) flow and lower density than the nearby unmodified solar wind, surrounded by a sheath of compressed plasma. In the quasi-parallel foreshock, it can prove difficult to separate these structures from the shock itself—in fact, a patchwork of SLAMS may completely replace the shock [Schwartz and Burgess, 1991]. Similar structures can form when IMF rotations interact with the shock.

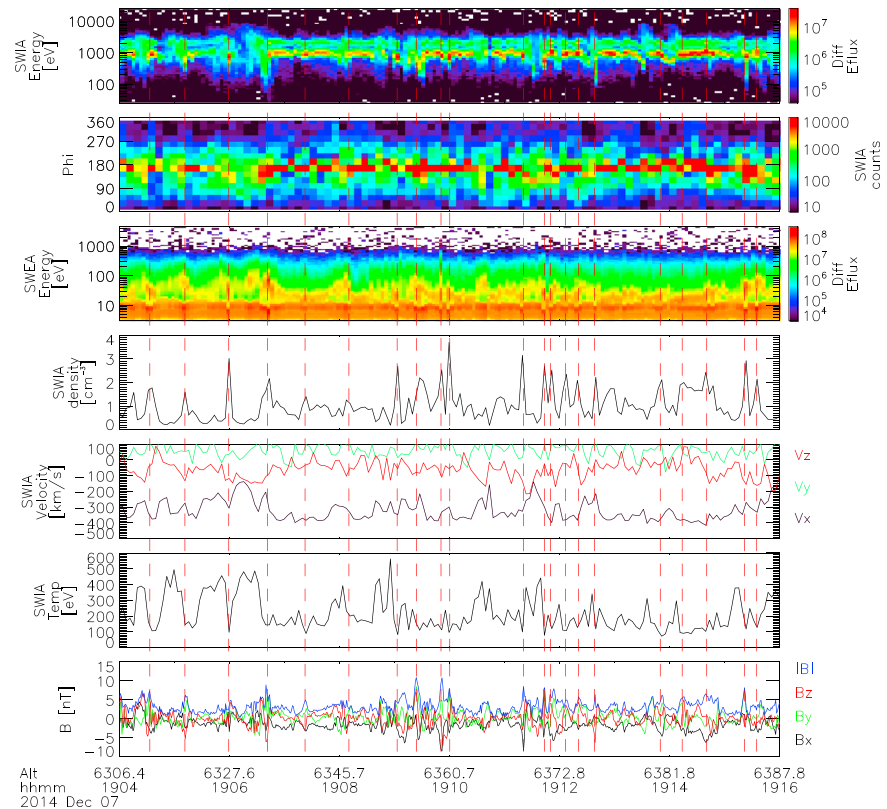
Hot flow anomalies (HFAs) [Schwartz *et al.*, 1985; Thomsen *et al.*, 1986], which form when a tangential discontinuity (TD) comes into contact with the bow shock in such a way that reflected ions are channeled toward the TD by the motional electric field [Schwartz, 1995; Thomas *et al.*, 1991], occur upstream from Earth, Venus [Collinson *et al.*, 2012], Mars [Collinson *et al.*, 2015], and Saturn [Masters *et al.*, 2009]. Related structures include foreshock bubbles (FBs) [Omidi *et al.*, 2010; Turner *et al.*, 2013] and spontaneous hot flow anomalies (SHFAs) [Omidi *et al.*, 2013; Zhang *et al.*, 2013]. All of these phenomena form as a result of nonlinear ion-ion interactions, occurring during both steady and changing IMF conditions.

Figure 14 shows SWIA, SWEA, and MAG data from a portion of an orbit on which MAVEN observed an isolated upstream event (1) and a group of repeated upstream events (2), both well upstream (2000–3000 km) from the bow shock (3). The observed structures have higher temperatures but lower densities and flow speeds than the surrounding solar wind, with strong compressional features visible in both the density and magnetic field on their upstream side (the side observed later in time, assuming that the structures convect over the spacecraft). On this orbit segment, MAVEN traveled from a point above the subsolar region of the magnetosphere to one just downstream from the terminator, with apoapsis to the southeast of the Mars-Sun line at an SZA of 72°. Much as in the time period of Figure 3, the upstream IMF had a near-radial orientation during this time, as indicated by the cone angle near 180°. For this IMF orientation, essentially the entire shock has a quasi-parallel geometry, making it easier for reflected ions from the shock to travel upstream over a large region and thereby favoring the formation of upstream structures. The isolated event appears to be associated with an IMF rotation, but the high-amplitude perturbations to the field around the repeated events preclude the identification of any IMF rotations associated with them.

During this time period, large fluxes of protons appear outside of the main solar wind beam, most clearly seen in Figure 14 (second panel). The fluxes, time dependence, and angular distributions of these ions indicate that they do not consist solely of solar wind scattered from the spacecraft or instrument but instead must include newly born ions from the Martian exosphere, reflected ions from the bow shock, and/or heated solar wind ions. For most of the time interval in question, the non-solar wind population extends over the entire instrument phi range, which given the Sun-pointing attitude (0° instrument phi = sunward) implies a contribution from protons (either solar wind or pickup hydrogen) reflected with sunward velocities from the shock or from ions scattered at large angles by wave-particle interactions. On the other hand, near the repeated group of events and inside the bow shock, the predominantly antisunward angular distribution of ion flux suggests that pickup ions, protons reflected from the shock at a glancing angle, and/or heated solar wind ions play a primary role. At these times, significantly heated populations of electrons also appear (Figure 14, third panel), providing observational support for the latter possibility. Ion and electron heating naturally occurs in the sheath downstream from the shock. However, upstream from the shock some other heating mechanism must operate, most likely driven directly or indirectly by ion-ion instabilities.

Figure 15 shows an expanded view of the group of repeated events of Figure 14. At this time the spacecraft has  $[X_{\text{MSO}}, Y_{\text{MSO}}, Z_{\text{MSO}}]$  coordinates of  $\sim[4000, 4000, -8000]$  km, upstream of the flank of the magnetosphere and to the southeast of the Mars-Sun line. MAVEN observes a number of quasi-periodic structures, with populations of almost normal solar wind interspersed with heated populations with lower density than the nearby solar wind and slowed and deflected (toward  $-Z_{\text{MSO}}$ , away from the Mars-Sun line) bulk flow. Most of these regions of hot tenuous plasma have a leading compression (with higher density and magnetic field than the undisturbed solar wind) at the upstream side. A few of the structures also appear to have trailing compressional regions, but most do not. The plasma in these structures, though strongly heated, still has a net anti-sunward bulk flow. The sunward reflected flux present in the surrounding time periods largely disappears during the interval shown in Figure 15, suggesting either that the structure of the bow shock downstream from the spacecraft has changed and/or that reflected protons from the downstream bow shock cannot penetrate these structures. Some antisunward (predominantly southward) flux does appear in the 45–90° instrument phi range, possibly consisting of protons reflected laterally from the portion of the shock to the north of the spacecraft and/or heated solar wind protons.

During most of the interval in Figure 14 we observe ULF waves near the proton cyclotron frequency. These could result from either newly born pickup hydrogen ions or reflected protons from the shock [Ruhunusiri *et al.*, 2016]. One might speculate on whether such waves could provide a seed population of fluctuations that grow into the nonlinear upstream events we observe. If so, since these waves vary seasonally as the



**Figure 15.** A subset of the measurements in Figure 14, covering a portion of the group of upstream events near time 2 in Figure 14. The panels show SWIA onboard-computed energy spectra and Coarse instrument phi angle spectra, SWEA electron energy spectra, density, velocity, and scalar temperature from SWIA onboard moments, and magnetic field components and magnitude. Ion and electron energy spectra utilize units of  $\text{eV}/(\text{eV cm}^2 \text{ s sr})$ , and vector quantities utilize the MSO coordinate system. Vertical dashed red lines mark the locations of density compressions. Text labels indicate the spacecraft altitude in kilometers.

hydrogen exosphere expands and contracts [Bertucci et al., 2013], this could lead to a seasonal variation in upstream event occurrence. Other parameters that could play a role include IMF cone angle and Mach number (for instance, small cone angles favor the growth of FBs [Omidi et al., 2010], and cone angle and Mach number affect the occurrence of and strength of the FCB [Omidi et al., 2009]). Finally, since solar wind dynamic pressure affects the shock location, we also considered this parameter.

To investigate the importance of these four parameters in determining when and where upstream events occur at Mars, we conducted a visual orbit-by-orbit search for similar isolated and repeated upstream events during December 2014 (near perihelion, with high EUV input and a large coronal hydrogen density) and August 2015 (farther from the Sun, with low EUV input and a low coronal hydrogen density). We defined isolated events as those that occurred more than 10 min before and after any other upstream event, while grouping together repeated events occurred within 10 min of each other. For several orbits, including the one shown in Figures 14 and 15, we identified 20 or more individual structures within in a single group of quasiperiodic repeated events.

Figure 16 shows the distribution of solar wind parameters for all upstream intervals as compared to those for the nearest undisturbed upstream times to the isolated and repeated upstream events we identified in the 2 months we investigated. We find similar occurrence rates of upstream events of both types in each of the 2 months, implying that EUV or other seasonal effects most likely do not play a major role. This in turn implies that the occurrence of strong upstream events does not require a seed population of waves produced by newly born pickup ions. Instead, it suggests that reflected protons from the shock play a dominant role. In addition, the spatial distribution of both isolated and repeated events (not shown) appears consistent with

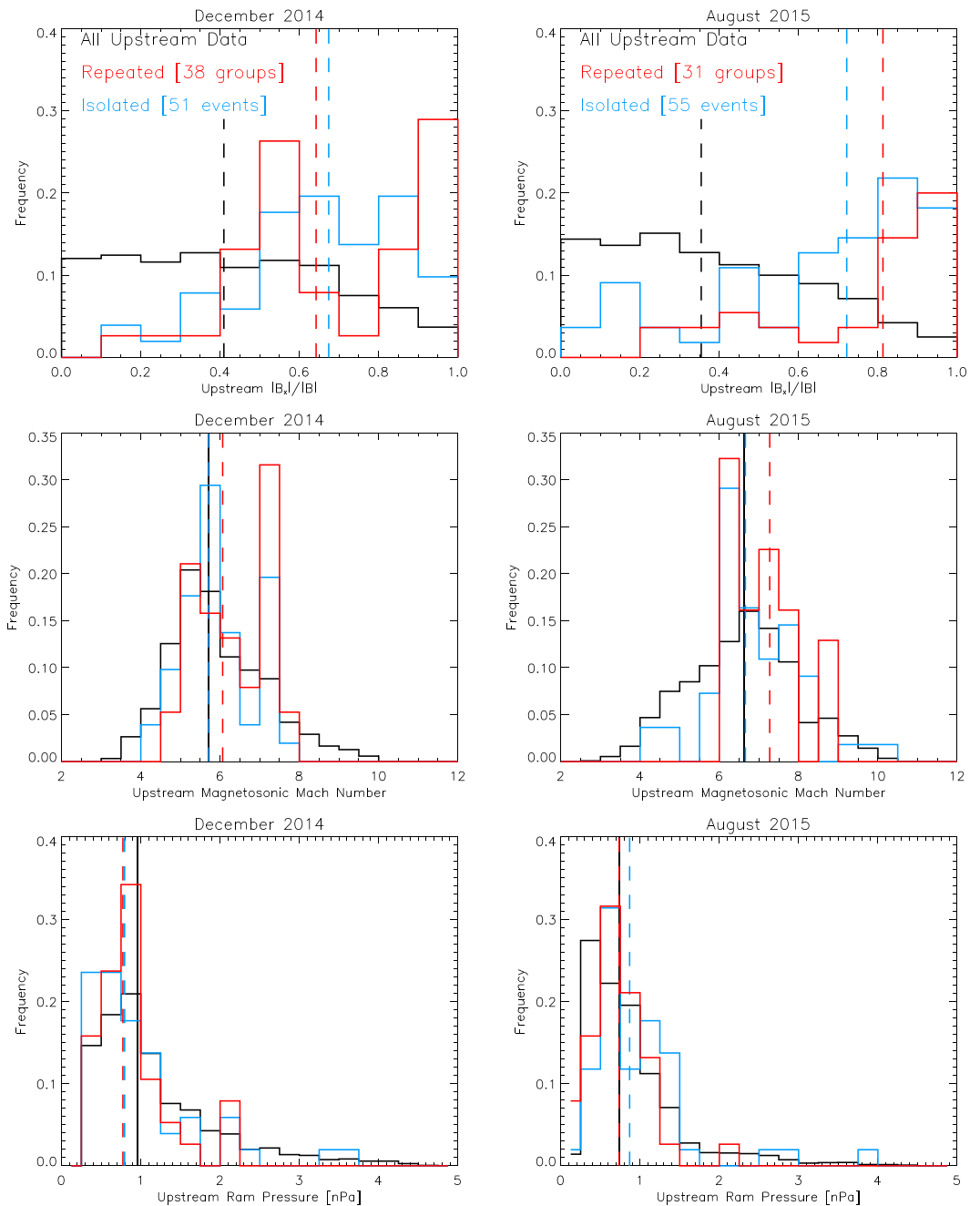


**Figure 16.** Distributions of three selected solar wind parameters from (left column) December 2014 and (right column) August 2015 in black, as compared to distributions of the same parameters from the nearest unperturbed upstream intervals to isolated upstream events (blue) and groups of repeated upstream events (red). (top row) Distributions of upstream  $|B_x|/|B|$  (the absolute value of the cosine of the IMF cone angle). (middle row) Distributions of solar wind magnetosonic Mach number. (bottom row) Distributions of solar wind dynamic pressure. All distributions utilize upstream measurements averaged over 45 s intervals. Vertical dashed lines indicate the median values for each distribution.

the overall frequency distribution of the measurements, implying that the observed structures commonly extend well upstream from the nominal bow shock location.

Of the solar wind parameters considered, only the IMF direction appears to play a major role. Near-radial IMF orientations heavily favor the occurrence of both isolated and repeated upstream events, during both time intervals considered. This controlling role for the IMF appears consistent with basic expectations, since in

radial IMF configurations reflected ions can access regions far upstream from Mars, favoring the growth of ion-ion instabilities. On the other hand, dynamic pressure appears to play no significant role and Mach number plays at most a minor role. Repeated events occur during conditions with median Mach numbers only 0.5–1 higher than the overall distribution of upstream measurements during the time periods in question. A future study should investigate whether solar wind parameters affect the magnitude of the observed upstream events, even if they do not affect their occurrence rate.

Based on the characteristics of the individual events and the statistics of their occurrence, the MAVEN observations may indicate SLAMS generated by ion reflection from the quasi-parallel shock. Under this interpretation, the upstream compression regions represent the SLAMS themselves, while the tenuous heated plasma downstream from these compressions represents the “wake” of the SLAMS [Hellinger and Mangeney, 1999; Behlke *et al.*, 2003]. The MAVEN observations, with large enhancements in both magnetic field and density, suggest a fast-mode structure, and the amplitude of the magnetic field enhancements appears consistent with previous observations of SLAMS [Schwartz *et al.*, 1992]. Wakes form because the SLAMS convect upstream in the frame of the undisturbed solar wind, resulting in a downstream wake region filled with hotter and more tenuous plasma (since only these particles can access this wake region), which may consist primarily of particles reflected from the shock and/or from other nearby SLAMS. In the frame of Mars, SLAMS convect downstream (albeit more slowly than the undisturbed solar wind) and steepen and pile up in the vicinity of the nominal bow shock. Much as at the Earth, a patchwork of SLAMS may essentially replace the Martian bow shock in the quasi-parallel geometry [Schwartz and Burgess, 1991].

We note that at Mars, a single SLAMS (assuming the same typical scales of several thousands of kilometers as seen at the Earth) could affect a substantial portion of the Martian bow shock, thereby altering the structure of the sheath and the magnetosphere. Therefore, the formation of a large number of quasi-periodic SLAMS could significantly affect the structure of the magnetosphere. At Venus, near-radial IMF orientations lead to large-scale disturbances in the magnetosphere [Zhang *et al.*, 2009] and significantly affect the loss of ions from the Venus system [Masunaga *et al.*, 2011]. The occurrence of upstream events under near-radial IMF could also dramatically change the dominant ion loss channels from the Martian system.

## 6. Conclusions and Implications

With no global internal magnetic field, the magnetosphere of Mars forms as a result of the direct and indirect interaction of the solar wind with the Martian ionosphere, through a combination of induction effects and mass loading. The resulting “induced magnetosphere” responds strongly to the influence of solar drivers, which vary as a function of solar cycle, heliocentric distance, and with solar rotation. Given the short MAVEN mission to date, we cannot yet comprehensively investigate solar cycle variations, but with 0.85 Martian years of nearly continuous observations, we can now investigate the influence of heliocentric distance and variability on solar rotation time scales.

The SWIA instrument returns direct measurements of the upstream solar wind drivers, as well as proxy measurements of the solar wind at periapsis enabled by the interaction between the solar wind and neutral atmospheric particles. Together, these two data sets provide nearly continuous monitoring of the solar wind during the MAVEN mission. The solar wind measurements provide one portion of the solar energy input to the Martian system, with other critical inputs measured by the SWEA, MAG, EUVM, and SEP instruments. When used appropriately, taking into account the effects of the mechanical attenuator and the telemetry mode, and correcting when necessary for the effects of penetrating and scattered backgrounds, limited energy-angle coverage, and multi-ion distributions, SWIA provides high-quality measurements of the solar wind density, velocity, temperature, and 3-D velocity distributions upstream from the bow shock and in the magnetosheath of Mars. These observations can be used to organize the data from other MAVEN instruments, including the critical measurements of ion escape from the Martian system [Brain *et al.*, 2015; Dong *et al.*, 2015].

The Martian bow shock and magnetosphere respond to the influence of both the highly variable solar wind and the less variable EUV input, while crustal magnetic fields play only a secondary role in determining the position of the bow shock. In agreement with previous observations, we find that high solar wind dynamic pressure and Mach number compress the bow shock, while high EUV inflates the shock [Edberg *et al.*, 2009, 2010a]. Both solar wind pressure and EUV vary inversely with heliocentric distance, leading to

competing influences on the Martian system. However, the high degree of variability in the solar wind still allows us to investigate the structure of the magnetosphere over a wide range of input parameters.

MAVEN observations also reveal variability in the energy input from Alfvén waves in the solar wind. We find some observable variation during the MAVEN mission of the normalized cross helicity of low-frequency fluctuations in solar wind magnetic field and velocity, which may result from a combination of heliocentric and solar cycle effects. If the analogy with the terrestrial system holds, these waves may affect the Martian magnetosphere and possibly even the thermosphere [Prikryl *et al.*, 2005].

SWIA observations also confirm a strong seasonal variation of the hydrogen corona [Yamauchi *et al.*, 2015; Chaffin *et al.*, 2014; Bhattacharyya *et al.*, 2015], with much larger (an order of magnitude) amplitude than the heliocentric variation in EUV input. A longer baseline of observations afforded by additional MAVEN extended missions could reveal a solar cycle component to the hydrogen variability or interannual variations in the seasonal variation of the hydrogen corona.

During most time periods, neither the presence of pickup ions from the hydrogen and oxygen corona nor the reflection of solar wind and/or pickup ions from the bow shock introduce significant perturbations to the solar wind upstream from Mars. MAVEN observes only weak mass loading signatures upstream from the bow shock and outside of the foreshock, producing velocity deflections of only  $\sim 5$  km/s even for low-density solar wind. An observed increase in the Alfvén ratio near the shock, indicating preferential transfer of energy to velocity fluctuations, may result from these mass-loading effects.

During periods of near-radial IMF, MAVEN often observes large-amplitude perturbations to the upstream flow, with factor of 2 or greater compressions of the density and magnetic field, interspersed with populations of hot tenuous plasma with lower flow speed. These perturbations likely result from the formation of SLAMS, together with their trailing wakes, generated by ion reflection from the bow shock and/or other SLAMS. As these large-scale structures convect downstream, they result in a global reconfiguration of the Martian bow shock and magnetosphere, with potential implications for ion escape during these time periods.

#### Acknowledgments

Analysis of SWEA data was partially supported by CNES. All MAVEN data are publicly available through the Planetary Data System (<http://ppi.pds.nasa.gov>). We thank two reviewers for carefully reading this long paper and providing constructive feedback that improved the manuscript.

#### References

- Acuña, M. H., *et al.* (1999), Global distribution of crustal magnetization found by the Mars Global Surveyor MAG/ER experiment, *Science*, *284*, 790–793, doi:10.1126/science.284.5415.790.
- Bale, S. D., F. S. Mozer, and T. S. Horbury (2003), Density-transition scale at quasiperpendicular collisionless shocks, *Phys. Rev. Lett.*, *91*, 265004, doi:10.1103/PhysRevLett.91.265004.
- Barabash, S., *et al.* (2006), The Analyzer of Space Plasmas and Energetic Atoms (ASPERA-3) for the Mars Express Mission, *Space Sci. Rev.*, *126*, 113–164, doi:10.1007/s11214-006-9124-8.
- Barabash, S., A. Fedorov, R. Lundin, and J. A. Sauvaud (2007), Martian atmospheric erosion rates, *Science*, *315*, 501–503, doi:10.1126/science.1134358.
- Bavassano, B., E. Pietropaolo, and R. Bruno (1998), Cross-helicity and residual energy in solar wind turbulence: Radial evolution and latitudinal dependence in the region from 1 to 5 AU, *J. Geophys. Res.*, *103*, 6521–6529, doi:10.1029/97JA03029.
- Behar, E., H. Nilsson, G. Stenberg Wieser, Z. Nemeth, T. W. Broiles, and I. Richter (2016), Mass loading at 67P/Churyumov-Gerasimenko: A case study, *Geophys. Res. Lett.*, *43*, 1411–1418, doi:10.1002/2015GL067436.
- Behlke, R., M. André, S. C. Buchert, A. Vaivads, A. I. Eriksson, E. A. Lucek, and A. Balogh (2003), Multi-point electric field measurements of Short Large-Amplitude Magnetic Structures (SLAMS) at the Earth's quasi-parallel bow shock, *Geophys. Res. Lett.*, *30*(4), 1177, doi:10.1029/2002GL015871.
- Belcher, J. W., and L. Davis Jr. (1971), Large amplitude Alfvén waves in the interplanetary medium, *2*, *J. Geophys. Res.*, *76*, 3534–3563, doi:10.1029/JA076i016p03534.
- Bertucci, C., C. Mazelle, M. H. Acua, C. T. Russell, and J. A. Slavin (2005), Structure of the magnetic pileup boundary at Mars and Venus, *J. Geophys. Res.*, *110*, A01209, doi:10.1029/2004JA010592.
- Bertucci, C., N. Romanelli, J. Y. Chaufray, D. Gomez, C. Mazelle, M. Delva, R. Modolo, F. González-Galindo, and D. A. Brain (2013), Temporal variability of waves at the proton cyclotron frequency upstream from Mars: Implications for Mars distant hydrogen exosphere, *Geophys. Res. Lett.*, *40*, 3809–3813, doi:10.1002/grl.50709.
- Bhattacharyya, D., J. T. Clarke, J.-L. Bertaux, J.-Y. Chaufray, and M. Mayyasi (2015), A strong seasonal dependence in the Martian hydrogen exosphere, *Geophys. Res. Lett.*, *42*, 8678–8685, doi:10.1002/2015GL065804.
- Blanco-Cano, X., N. Omid, and C. T. Russell (2009), Global hybrid simulations: Foreshock waves and cavitons under radial interplanetary magnetic field geometry, *J. Geophys. Res.*, *114*, A01216, doi:10.1029/2008JA013406.
- Bougher, S. W., *et al.* (2015), Early MAVEN Deep Dip campaign reveals thermosphere and ionosphere variability, *Science*, *350*, 0459, doi:10.1126/science.aad0459.
- Brain, D. A., F. Bagenal, M. H. Acuña, J. E. P. Connerney, D. H. Crider, C. Mazelle, D. L. Mitchell, and N. F. Ness (2002), Observations of low-frequency electromagnetic plasma waves upstream from the Martian shock, *J. Geophys. Res.*, *107*(A6), 1076, doi:10.1029/2000JD000416.
- Brain, D. A., J. S. Halekas, R. J. Lillis, D. L. Mitchell, R. P. Lin, and D. H. Crider (2005), Variability of the altitude of the Martian sheath, *Geophys. Res. Lett.*, *32*, L18203, doi:10.1029/2005GL023126.
- Brain, D. A., R. J. Lillis, D. L. Mitchell, J. S. Halekas, and R. P. Lin (2007), Electron pitch angle distributions as indicators of magnetic field topology near Mars, *J. Geophys. Res.*, *112*, A09201, doi:10.1029/2007JA012435.

- Brain, D. A., et al. (2015), The spatial distribution of planetary ion fluxes near Mars observed by MAVEN, *Geophys. Res. Lett.*, *42*, 9142–9148, doi:10.1002/2015GL065293.
- Breech, B., W. H. Matthaeus, J. Minnie, S. Oughton, S. Parhi, J. W. Bieber, and B. Bavassano (2005), Radial evolution of cross-helicity in the high-latitude solar wind, *Geophys. Res. Lett.*, *32*, L016103, doi:10.1029/2004GL022321.
- Bruno, R., and V. Carbone (2005), The solar wind as a turbulence laboratory, *Living Rev. Sol. Phys.*, *2*, doi:10.12942/lrsp-2013-2.
- Burlaga, L. F., V. Pizzo, A. Lazarus, and P. Gazis (1985), Stream dynamics between 1 AU and 2 AU: A comparison of observations and theory, *J. Geophys. Res.*, *90*, 7377–7388, doi:10.1029/JA090iA08p07377.
- Burgess, D., et al. (2005), Quasi-parallel shock structure and processes, *Space Sci. Rev.*, *118*, 205–222, doi:10.1007/s11214-005-3832-3.
- Carlson, C. W., D. W. Curtis, G. Paschmann, and W. Michael (1983), An instrument for rapidly measuring plasma distribution functions with high resolution, *Adv. Space Res.*, *2*, 67–70, doi:10.1016/0273-1177(82)90151-X.
- Chaffin, M. S., J.-Y. Chaufray, I. Stewart, F. Montmessin, N. M. Schneider, and J.-L. Bertaux (2014), Unexpected variability of Martian hydrogen escape, *Geophys. Res. Lett.*, *41*, 314–320, doi:10.1002/2013GL058578.
- Collinson, G. A., et al. (2012), Hot flow anomalies at Venus, *J. Geophys. Res.*, *117*, A04204, doi:10.1029/2011JA017277.
- Collinson, G., et al. (2015), A hot flow anomaly at Mars, *Geophys. Res. Lett.*, *42*, 9121–9127, doi:10.1002/2015GL065079.
- Connerney, J., J. Espley, P. Lawton, S. Murphy, J. Odom, R. Oliverson, and D. Sheppard (2015a), The MAVEN magnetic field investigation, *Space Sci. Rev.*, doi:10.1007/s11214-015-0169-4.
- Connerney, J. E. P., J. R. Espley, G. A. DiBraccio, J. R. Gruesbeck, R. J. Oliverson, D. L. Mitchell, J. Halekas, C. Mazelle, D. Brain, and B. M. Jakosky (2015b), First results of the MAVEN magnetic field investigation, *Geophys. Res. Lett.*, *42*, 8819–8827, doi:10.1002/2015GL065366.
- Corder, G. W., and D. I. Foreman (2014), *Nonparametric Statistics: A Step-by-Step Approach*, John Wiley, Hoboken, N. J.
- DiBraccio, G. A., et al. (2015), Magnetotail dynamics at Mars: Initial MAVEN observations, *Geophys. Res. Lett.*, *42*, 8828–8837, doi:10.1002/2015GL065248.
- Dong, Y., X. Fang, D. A. Brain, J. P. McFadden, J. S. Halekas, J. E. Connerney, S. Curry, Y. Harada, J. G. Luhmann, and B. M. Jakosky (2015), Strong plume fluxes at Mars observed by MAVEN: An important planetary ion escape channel, *Geophys. Res. Lett.*, *42*, 8942–8950, doi:10.1002/2015GL065346.
- Dubinin, E., R. Lundin, O. Norberg, and N. Pissarenko (1993a), Ion acceleration in the Martian tail: Phobos observations, *J. Geophys. Res.*, *98*, 3991–3997, doi:10.1029/92JA02233.
- Dubinin, E., R. Lundin, H. Koskinen, and O. Norberg (1993b), Cold ions at the Martian bow shock: Phobos observations, *J. Geophys. Res.*, *98*, 5617–5623, doi:10.1029/92JA02374.
- Dubinin, E., K. Sauer, M. Delva, S. Livi, R. Lundin, A. Skalsky, and K. Szego (2000), Deceleration of the solar wind upstream of the Martian bow shock. Mass-loading or foreshock features?, *Adv. Space Res.*, *26*, 1627–1631, doi:10.1016/S0273-1177(00)00104-6.
- Dubinin, E., M. Franz, J. Woch, E. Roussos, S. Barabash, R. Lundin, J. D. Winningham, R. A. Frahm, and M. Acuna (2006a), Plasma morphology at Mars: ASPERA-3 observations, *Space Sci. Rev.*, *126*, 209–238, doi:10.1007/s11214-006-9039-4.
- Dubinin, E., M. Fraenz, J. Woch, S. Barabash, R. Lundin, and M. Yamauchi (2006b), Hydrogen exosphere at Mars: Pickup protons and their acceleration at the bow shock, *Geophys. Res. Lett.*, *33*, L22103, doi:10.1029/2006GL027799.
- Dubinin, E., et al. (2008), Structure and dynamics of the solar wind/ionosphere interface on Mars: MEX-ASPERA-3 and MEX-MARSIS observations, *Geophys. Res. Lett.*, *35*, L11103, doi:10.1029/2008GL033730.
- Dubinin, E., M. Fraenz, J. Woch, F. Duru, D. Gurnett, R. Modolo, S. Barabash, and R. Lundin (2009), Ionospheric storms on Mars: Impact of the corotating interaction region, *Geophys. Res. Lett.*, *36*, L01105, doi:10.1029/2008GL036559.
- Dubinin, E., M. Fraenz, A. Fedorov, R. Lundin, N. Edberg, F. Duru, and O. Vaisberg (2011), Ion energization and escape on Mars and Venus, *Space Sci. Rev.*, *162*, 173, doi:10.1007/s11214-011-9831-7.
- Eastwood, J. P., E. A. Lucek, C. Mazelle, K. Meziane, Y. Narita, J. Pickett, and R. A. Treumann (2005), The foreshock, *Space Sci. Rev.*, *118*, 41–94, doi:10.1007/s11214-005-3824-3.
- Edberg, N., D. A. Brain, M. Lester, S. W. H. Cowley, R. Modolo, M. Fraenz, and S. Barabash (2009), Plasma boundary variability at Mars as observed by Mars Global Surveyor and Mars Express, *Ann. Geophys.*, *27*, 3537–3550, doi:10.5194/angeo-27-3537-2009.
- Edberg, N. J. T., M. Lester, S. W. H. Cowley, and A. I. Eriksson (2008), Statistical analysis of the location of the Martian magnetic pileup boundary and bow shock and the influence of crustal magnetic fields, *J. Geophys. Res.*, *113*, A08206, doi:10.1029/2008JA013096.
- Edberg, N. J. T., M. Lester, S. W. H. Cowley, D. A. Brain, M. Franz, and S. Barabash (2010a), Magnetosonic Mach number effect of the position of the bow shock at Mars in comparison to Venus, *J. Geophys. Res.*, *115*, A07203, doi:10.1029/2009JA014998.
- Edberg, N. J. T., H. Nilsson, A. O. Williams, M. Lester, S. E. Milan, S. W. H. Cowley, M. Franz, S. Barabash, and Y. Futaana (2010b), Pumping out the atmosphere of Mars through solar wind pressure pulses, *Geophys. Res. Lett.*, *37*, L03107, doi:10.1029/2009GL041814.
- Eparvier, F. G., et al. (2015), The Solar Extreme Ultraviolet Monitor for MAVEN, *Space Sci. Rev.*, *195*, 293–301, doi:10.1007/s11214-015-0195-2.
- Ergun, R. E., L. Andersson, W. K. Peterson, D. Brain, G. T. Delory, D. L. Mitchell, R. P. Lin, and A. W. Yau (2006), Role of plasma waves in Mars' atmospheric loss, *Geophys. Res. Lett.*, *33*, L14103, doi:10.1029/2006GL025785.
- Espley, J. R., P. A. Cloutier, D. A. Brain, D. H. Crider, and M. H. Acuña (2004), Observations of low-frequency magnetic oscillations in the Martian magnetosheath, magnetic pileup region, and tail, *J. Geophys. Res.*, *109*, A07213, doi:10.1029/2003JA010193.
- Fraenz, M., E. Dubinin, E. Roussos, J. Woch, J. D. Winningham, R. Frahm, A. J. Coates, A. Fedorov, S. Barabash, and R. Lundin (2006), Plasma moments in the environment of Mars, *Space Sci. Rev.*, *126*, 165–207, doi:10.1007/s11214-006-9115-9.
- Fraenz, M., E. Dubinin, D. Andrews, S. Barabash, H. Nilsson, and A. Fedorov (2015), Cold ion escape from the Martian ionosphere, *Planet. Space Sci.*, *119*, 92–102, doi:10.1016/j.pss.2015.07.012.
- Futaana, Y., et al. (2008), Mars Express and Venus Express multi-point observations of geoeffective solar flare events in December 2006, *Planet. Space Sci.*, *56*, 873–880, doi:10.1016/j.pss.2007.10.014.
- Gary, S. P. (1991), Electromagnetic ion/ion instabilities and their consequence in space plasmas: A review, *Space Sci. Rev.*, *56*, 373–415, doi:10.1007/BF00196632.
- Goldstein, B. E., M. Neugebauer, and E. J. Smith (1995), Alfvén waves, alpha particles, and pickup ions in the solar wind, *Geophys. Res. Lett.*, *22*, 3389, doi:10.1029/95GL03182.
- Goldstein, R., et al. (2015), The Rosetta Ion and Electron Sensor (IES) measurement of the development of pickup ions from comet 67P/Churyumov-Gerasimenko, *Geophys. Res. Lett.*, *42*, 3093–3099, doi:10.1002/2015GL063939.
- Gosling, J. T., and V. J. Pizzo (1999), Formation and evolution of corotating interaction regions and their three dimensional structure, in *Corotating Interaction Regions*, pp. 21–52, Springer, Netherlands.
- Gunell, H., et al. (2008), Shear driven waves in the induced magnetosphere of Mars, *Plasma Phys. Contr. Fusion*, *50*, doi:10.1088/0741-3335/50/7/074018.
- Halekas, J. S., E. R. Taylor, G. Dalton, G. Johnson, D. W. Curtis, J. P. McFadden, D. L. Mitchell, R. P. Lin, and B. M. Jakosky (2015a), The Solar Wind Ion Analyzer for MAVEN, *Space Sci. Rev.*, doi:10.1007/s11214-013-0029-z.

- Halekas, J. S., J. P. McFadden, J. E. P. Connerney, J. R. Espley, D. A. Brain, D. L. Mitchell, D. E. Larson, Y. Harada, T. Hara, and S. Ruhunusiri (2015b), Time-dispersed ion signatures observed in the Martian magnetosphere by MAVEN, *Geophys. Res. Lett.*, **42**, 8910–8916, doi:10.1002/2015GL064781.
- Halekas, J. S., et al. (2015c), MAVEN observations of solar wind hydrogen deposition in the atmosphere of Mars, *Geophys. Res. Lett.*, **42**, 8901–8909, doi:10.1002/2015GL064693.
- Halekas, J. S., et al. (2016), Plasma clouds and snowplows: Bulk plasma escape from Mars observed by MAVEN, *Geophys. Res. Lett.*, **43**, 1426–1434, doi:10.1002/2016GL067752.
- Haerendel, G., G. Paschmann, W. Baumjohann, and C. W. Carlson (1986), Dynamics of the AMPTE artificial comet, *Nature*, **320**, 720–723, doi:10.1038/320720a0.
- Harada, Y., et al. (2015), Marsward and tailward ions in the near-Mars magnetotail: MAVEN observations, *Geophys. Res. Lett.*, **42**, 8925–8932, doi:10.1002/2015GL065005.
- Hellinger, P., and A. Mangeney (1999), Electromagnetic ion beam instabilities: Oblique pulsations, *J. Geophys. Res.*, **104**, 4669, doi:10.1029/1998JA900157.
- Ip, W.-H., and W. I. Axford (1982), Theories of physical processes in the cometary comae and ion terrestrial, in *Comets*, edited by L. L. Wilkening, 588 pp., Univ. Arizona Press, Tucson.
- Jakosky, B. M., et al. (2015a), The Mars Atmosphere and Volatile Evolution (MAVEN) mission, *Space Sci. Rev.*, doi:10.1007/s11214-015-0139-x.
- Jakosky, B. M., et al. (2015b), MAVEN observations of the response of Mars to an interplanetary coronal mass ejection, *Science*, **350**, 0210, doi:10.1126/science.aad3443.
- Kallio, E., and S. Barabash (2001), Atmospheric effects of precipitating energetic hydrogen atoms on the Martian atmosphere, *J. Geophys. Res.*, **106**, 165–177, doi:10.1029/2000JA002003.
- Kallio, E., J. G. Luhmann, and S. Barabash (1997), Charge exchange near Mars: Solar wind absorption and energetic neutral atom production, *J. Geophys. Res.*, **102**, 22,183–22,197, doi:10.1029/97JA01662.
- Kotova, G., et al. (1997), Study of the solar wind deceleration upstream of the Martian terminator bow shock, *J. Geophys. Res.*, **102**, 2165–2173, doi:10.1029/96JA01533.
- Larson, D. E., et al. (2015), The MAVEN solar energetic particle investigation, *Space Sci. Rev.*, **195**, 153–172, doi:10.1007/s11214-015-0218-z.
- Leblanc, F., and R. E. Johnson (2001), Sputtering of the Martian atmosphere by solar wind pick-up ions, *Planet. Space Sci.*, **49**, 645–656, doi:10.1016/S0032-0633(01)00003-4.
- Lundin, R., B. Hultqvist, S. Olsen, A. Zakharov, N. Pissarenko, E. Dubinin, R. Pellinen, and I. Liede (1989), The ASPERA experiment on the soviet Phobos spacecraft, in *Solar System Plasma Physics, American Geophysics Union Monograph No 54*, edited by J. H. Waite, J. Burch, and T. E. Moore, AGU, Washington, D. C.
- Lundin, R., A. Zakharov, R. Pellinen, S. W. Barabash, H. Borg, E. M. Dubinin, B. Hultqvist, H. Koskinen, I. Liede, and N. Pissarenko (1990), ASPERA/Phobos measurements of the ion outflow from the Martian ionosphere, *Geophys. Res. Lett.*, **17**, 873–876, doi:10.1029/GL017i006p00873.
- Lundin, R., E. M. Dubinin, H. Koskinen, O. Norberg, N. Pissarenko, and S. W. Barabash (1991), On the momentum transfer of the solar wind to the Martian topside ionosphere, *Geophys. Res. Lett.*, **18**, 1059, doi:10.1029/90GL02604.
- Lundin, R., S. Barabash, M. Holmstrom, H. Nilsson, M. Yamauchi, M. Fraenz, and E. M. Dubinin (2008), A comet-like escape of ionospheric plasma from Mars, *Geophys. Res. Lett.*, **35**, L18203, doi:10.1029/2008GL034811.
- Luhmann, J. G. (1995), Plasma interactions with unmagnetized bodies, in *Introduction to Space Physics*, edited by M. G. Kivelson and C. T. Russell, Cambridge Univ. Press, Cambridge, U. K.
- Luhmann, J. G., and J. U. Kozyra (1991), Dayside pickup oxygen ion precipitation at Venus and Mars: Spatial distributions, energy deposition and consequences, *J. Geophys. Res.*, **96**, 5457–5467, doi:10.1029/90JA01753.
- Masters, A., et al. (2009), Hot flow anomalies at Saturn's bow shock, *J. Geophys. Res.*, **114**, A08217, doi:10.1029/2009JA014112.
- Masunaga, K., Y. Futaana, M. Yamauchi, S. Barabash, T. L. Zhang, A. O. Fedorov, N. Terada, and S. Okano (2011), O<sup>+</sup> outflow channels around Venus controlled by directions of the interplanetary magnetic field: Observations of high energy O<sup>+</sup> ions around the terminator, *J. Geophys. Res.*, **116**, A09326, doi:10.1029/2011JA016705.
- Mazelle, C., et al. (2004), Bow shock and upstream phenomena at Mars, *Space Sci. Rev.*, **111**, 115–181, doi:10.1023/B:SPAC.0000032717.98679.d0.
- McComas, D. J., et al. (2016), Pluto's interaction with the solar wind, *J. Geophys. Res. Space Physics*, **121**, 4232–4246, doi:10.1002/2016JA022599.
- McFadden, J., et al. (2015), The MAVEN Suprathermal and thermal Ion Composition (STATIC) instrument, *Space Sci. Rev.*, **195**, 199–256, doi:10.1007/s11214-015-0175-6.
- Mitchell, D. L., et al. (2016), The MAVEN solar wind electron analyzer, *Space Sci. Rev.*, **200**, 495, doi:10.1007/s11214-015-0232-1.
- Nagy, A. F., et al. (2004), The plasma environment of Mars, *Space Sci. Rev.*, **111**, 33, doi:10.1023/B:SPAC.0000032718.47512.92.
- Nilsson, H., N. J. T. Edberg, G. Stenberg, S. Barabash, M. Holmström, Y. Futaana, R. Lundin, and A. Fedorov (2011), Heavy ion escape from Mars, influence from solar wind conditions and crustal magnetic fields, *Icarus*, **215**, 475–484, doi:10.1016/j.icarus.2011.08.003.
- Nilsson, H., et al. (2015), Evolution of the ion environment of comet 67P/Churyumov-Gerasimenko—Observations between 3.6 and 2.2 AU, *Astron. Astrophys.*, **538**, A20, doi:10.1051/0004-6361/201526142.
- Øieroset, M., D. L. Mitchell, T. D. Phan, R. P. Lin, and M. H. Acuña (2001), Hot diamagnetic cavities upstream of the Martian bow shock, *Geophys. Res. Lett.*, **28**, 887–890, doi:10.1029/2000GL012289.
- Omidi, N., D. G. Sibeck, and X. Blanco-Cano (2009), Foreshock compressional boundary, *J. Geophys. Res.*, **114**, A08205, doi:10.1029/2008JA013950.
- Omidi, N., J. P. Eastwood, and D. G. Sibeck (2010), Foreshock bubbles and their global magnetospheric impacts, *J. Geophys. Res.*, **115**, A06204, doi:10.1029/2009JA014828.
- Omidi, N., H. Zhang, D. G. Sibeck, and D. Turner (2013), Spontaneous hot flow anomalies at quasi-parallel shocks: 2. Hybrid simulations, *J. Geophys. Res. Space Physics*, **118**, 173–180, doi:10.1029/2012JA018099.
- Opitz, A., A. Fedorov, P. Wurz, K. Szego, J.-A. Sauvaud, R. Karrer, A. B. Galvin, S. Barabash, and F. Ipavich (2010), Solar wind bulk velocity throughout the inner heliosphere from multi-spacecraft measurements, *Solar Phys.*, **264**, 377–382, doi:10.1007/s11207-010-9583-7.
- Penz, T., et al. (2004), Ion loss on Mars caused by the Kelvin-Helmholtz instability, *Planet. Space Sci.*, **52**, 1157–1167, doi:10.1016/j.pss.2004.06.001.
- Perri, S., and A. Balogh (2010), Differences in solar wind cross-helicity and residual energy during the last two solar minima, *Geophys. Res. Lett.*, **37**, L17102, doi:10.1029/2010GL044570.

- Prikryl, P., D. B. Muldrew, G. J. Sofko, and J. M. Ruohoniemi (2005), Solar wind Alfvén waves: A source of pulsed ionospheric convection and atmospheric gravity waves, *Ann. Geophys.*, *23*, 401–417, doi:10.5194/angeo-23-401-2005.
- Rahmati, A., D. E. Larson, T. E. Cravens, R. J. Lillis, P. A. Dunn, J. S. Halekas, J. E. Connerney, F. G. Eparvier, E. M. B. Theimann, and B. M. Jakosky (2015), MAVEN insights into oxygen pickup ions at Mars, *Geophys. Res. Lett.*, *42*, 8870, doi:10.1002/2015GL065262.
- Rahmati, A., et al. (2017), MAVEN measured oxygen and hydrogen pickup ions: Probing the Martian exosphere and neutral escape, *J. Geophys. Res. Space Physics*, *122*, doi:10.1002/2016JA023371, in press.
- Ramstad, R., Y. Futaana, S. Barabash, H. Nilsson, S. M. del Campo Barraza, R. Lundin, and K. Schwingenschuh (2013), Phobos 2/ASPERA data revisited: Planetary ion escape rate from Mars near the 1989 solar maximum, *Geophys. Res. Lett.*, *40*, 477–481, doi:10.1002/grl.50149.
- Ramstad, R., S. Barabash, Y. Futaana, H. Nilsson, X.-D. Wang, and M. Holmstrom (2015), The Martian atmospheric ion escape rate dependence on solar wind and solar EUV conditions: 1. Seven years of Mars Express observations, *J. Geophys. Res. Planets*, *120*, 1298–1309, doi:10.1002/2015JE004816.
- Richardson, J. D., J. W. Belcher, A. J. Lazarus, K. I. Paularena, and P. R. Gazis (1996), Statistical properties of the solar wind, in *Proceedings of the Eighth International Solar Wind Conference*, pp. 483–486, American Institute of Physics, Melville, New York.
- Roberts, D. A., M. L. Goldstein, L. W. Klein, and W. H. Matthaeus (1987), Origin and evolution of fluctuations in the solar wind: Helios observations and Helios-Voyager comparisons, *J. Geophys. Res.*, *92*, 12,023, doi:10.1029/JA092iA11p12023.
- Romanelli, N., et al. (2016), Proton cyclotron waves occurrence rate upstream from Mars observed by MAVEN: Associated variability of the Martian upper atmosphere, *J. Geophys. Res. Space Physics*, *121*, 11,113–11,128, doi:10.1002/2016JA023270.
- Rosenbauer, H., et al. (1989), The study of three-dimensional distribution functions of the main solar wind ions—Protons and alpha particles in Phobos mission. TAUS experiment, in *The Instrumentation and Methods of Space Research*, edited by V. M. Balebanov, pp. 30–43, Nauka, Moscow.
- Ruhunusiri, S., J. S. Halekas, J. E. P. Connerney, J. R. Easley, J. P. McFadden, D. E. Larson, D. L. Mitchell, C. Mazelle, and B. M. Jakosky (2015), Low-frequency waves in the Martian magnetosphere and their response to upstream solar wind driving conditions, *Geophys. Res. Lett.*, *42*, 8917–8924, doi:10.1002/2015GL064968.
- Ruhunusiri, S., et al. (2016), MAVEN observation of an obliquely propagating low-frequency wave upstream from Mars, *J. Geophys. Res. Space Physics*, *121*, 2374–2389, doi:10.1002/2015JA022306.
- Russell, C. T., and M. Hoppe (1983), Upstream waves and particles, *Space Sci. Rev.*, *34*, 155–172, doi:10.1007/BF00194624.
- Russell, C. T., and R. J. Walker (1995), The magnetospheres of the outer planets, in *Introduction to Space Physics*, edited by M. G. Kivelson and C. T. Russell, pp. 503–519, Cambridge Univ. Press, Cambridge, U. K.
- Russell, C. T., J. G. Luhmann, K. Schwingenschuh, W. Riedler, and Y. Yeroshenko (1990), Upstream waves at Mars: Phobos observations, *Geophys. Res. Lett.*, *17*, 897–900, doi:10.1029/GL017i006p00897.
- Schwartz, S. J. (1995), Hot flow anomalies near the Earth's bow shock, *Adv. Space Res.*, *15*, 107–116, doi:10.1016/0273-1177(94)00092-F.
- Schwartz, S. J., and D. Burgess (1991), Quasi-parallel shocks: A patchwork of three-dimensional structures, *Geophys. Res. Lett.*, *18*, 373, doi:10.1029/91GL00138.
- Schwartz, S. J., C. P. Chaloner, D. S. Hall, P. J. Christiansen, and A. D. Johnstone (1985), An active current sheet in the solar wind, *Nature*, *318*, 269–271, doi:10.1038/318269a0.
- Schwartz, S. J., D. Burgess, W. P. Wilkinson, R. L. Kessel, M. Dunlop, and H. Lühr (1992), Observations of short large-amplitude magnetic structures at a quasi-parallel shock, *J. Geophys. Res.*, *97*, 4209, doi:10.1029/91JA02581.
- Sibeck, D. G., T.-D. Phan, R. Lin, R. P. Lepping, and A. Szabo (2002), Wind observations of foreshock cavities: A case study, *J. Geophys. Res.*, *107*(A10), 1271, doi:10.1029/2001JA007539.
- Slavin, J. A., K. Schwingenschuh, W. Riedler, and E. Eroshenko (1991), The solar wind interaction with Mars: Mariner 4, Mars 2, Mars 3, Mars 5 and PHOBOS 2 observations of bow shock position and shape, *J. Geophys. Res.*, *96*, 11,235–11,241, doi:10.1029/91JA00439.
- Steckiewicz, M., et al. (2015), Altitude dependence of nightside Martian suprathermal electron depletions as revealed by MAVEN observations, *Geophys. Res. Lett.*, *42*, 8877–8884, doi:10.1002/2015GL065257.
- Szego, K., et al. (2000), Physics of mass loaded plasmas, *Space Sci. Rev.*, *94*, 429–671.
- Szucs, I.-T., et al. (1990), The HARP electron and ion sensor on the Phobos mission, *Nucl. Instrum. Methods Phys. Res., Sect. A*, *290*, 228–236.
- Tatrallyay, M., G. Gévai, I. Apáthy, K. Schwingenschuh, T.-L. Zhang, G. A. Kotova, M. I. Verigin, S. Livi, and H. Rosenbauer (1997), Magnetic field overshoots in the Martian bow shock, *J. Geophys. Res.*, *102*, 2157, doi:10.1029/96JA00073.
- Thomas, V. A., D. Winske, M. F. Thomsen, and T. G. Onsager (1991), Hybrid simulation of the formation of a hot flow anomaly, *J. Geophys. Res.*, *96*, 11,625, doi:10.1029/91JA01092.
- Thomsen, M. F., J. T. Gosling, S. A. Fuselier, S. J. Bame, and C. T. Russell (1986), Hot, diamagnetic cavities upstream from the Earth's bow shock, *J. Geophys. Res.*, *91*, 2961–2973, doi:10.1029/JA091iA03p02961.
- Thomsen, M. F., J. T. Gosling, S. J. Bame, and C. T. Russell (1990), Magnetic pulsations at the quasi-parallel shock, *J. Geophys. Res.*, *95*, 957–966, doi:10.1029/JA095iA02p00957.
- Trotignon, J., C. Mazelle, C. Bertucci, and M. Acuña (2006), Martian shock and magnetic pile-up boundary positions and shapes determined from the Phobos 2 and Mars Global Surveyor data sets, *Planet. Space Sci.*, *54*(4), 357–369, doi:10.1016/j.pss.2006.01.003.
- Tu, C.-Y., and E. Marsch (1991), A case study of very low cross-helicity fluctuations in the solar wind, *Ann. Geophys.*, *9*, 319.
- Turner, D. L., N. Omid, D. G. Sibeck, and V. Angelopoulos (2013), First observation of foreshock bubbles upstream of Earth's bow shock: Characteristics and comparisons to HFAs, *J. Geophys. Res. Atmos.*, *118*, 1552–1570, doi:10.1002/jgra.50198.
- Verigin, M. I., K. I. Gringauz, G. Kotova, N. Shutte, H. Rosenbauer, S. Livi, A. K. Richter, W. Riedler, K. Schwingenschuh, and K. Szego (1991), On the problem of the Martian atmosphere dissipation: Phobos-2 TAUS spectrometer results, *J. Geophys. Res.*, *96*, 19,315, doi:10.1029/90JA02561.
- Verigin, M. I., et al. (1993), The dependence of the Martian magnetopause and bow shock on solar wind ram pressure according to Phobos 2 TAUS ion spectrometer measurements, *J. Geophys. Res.*, *98*, 1303–1309, doi:10.1029/92JA01666.
- Verigin, M. I., et al. (1999), Shape and location of planetary bow shocks, *Cosmic Res.*, *37*, 34.
- Vignes, D., C. Mazelle, H. Rme, M. H. Acuña, J. E. P. Connerney, R. P. Lin, D. L. Mitchell, P. Cloutier, D. H. Crider, and N. F. Ness (2000), The solar wind interaction with Mars: Locations and shapes of the bow shock and the magnetic pile-up boundary from the observations of the MAG/ER Experiment onboard Mars Global Surveyor, *Geophys. Res. Lett.*, *27*, 49–52, doi:10.1029/1999GL010703.
- Vignes, D., M. H. Acuña, J. E. P. Connerney, D. H. Crider, C. Mazelle, and H. Rème (2002), Factors controlling the location of the bow shock at Mars, *Geophys. Res. Lett.*, *29*(9), 1328, doi:10.1029/2001GL014513.
- Winningham, J. D., et al. (2006), Electron oscillations in the induced Martian magnetosphere, *Icarus*, *182*, 360, doi:10.1016/j.icarus.2005.10.033.

- Yamauchi, M., et al. (2015), Seasonal variation of Martian pick-up ions: Evidence of breathing exosphere, *Planet. Space Sci.*, doi:10.1016/j.pss.2015.09.013.
- Zhang, H., D. G. Sibeck, Q.-G. Zong, N. Omid, D. Turner, and L. B. N. Clausen (2013), Spontaneous hot flow anomalies at quasi-parallel shocks: 1. Observations, *J. Geophys. Res. Space Physics*, *118*, 3357–3363, doi:10.1002/jgra.50376.
- Zhang, T. L., J. Du, Y. J. Ma, H. Lammer, W. Baumjohann, C. Wang, and C. T. Russell (2009), Disappearing induced magnetosphere at Venus: Implications for close-in exoplanets, *Geophys. Res. Lett.*, *36*, L20203, doi:10.1029/2009GL040515.